Advancing Our Understanding of Martian Proton Aurora through a Coordinated Multi-Model Comparison Campaign

Andrea C. G. Hughes[1], Michael Scott Chaffin[2], Edwin J. Mierkiewicz[3], Justin Deighan[2], Rebecca Jolitz[4], Esa Kallio[5], Guillaume Gronoff[6], Valery I. Shematovich[7], Dmitry Bisikalo[7], Cyril L. Simon Wedlund[8], Jasper S. Halekas[9], Nicholas M. Schneider[10], Birgit Ritter[11], Zachary Girazian[12], Sonal Jain[2], Jean-Claude M. C. Gérard[13], and Bradley Michael Hegyi[14]

[1]NASA Goddard Space Flight Center / Howard University
[2]LASP
[3]Embry-Riddle Aeronautical University
[4]Laboratory of Atmospheric and Space Physics
[5]Aalto University, School of Electrical Engineering
[6]Nasa Langley Research Center
[7]Institute of Astronomy of the Russian Academy of Sciences
[8]Space Research Institute, OEAW
[9]University of Iowa
[10]University of Colorado Boulder
[11]Royal Observatory of Belgium
[12]The University of Iowa
[13]Université de Liège
[14]NASA Langley Research Center

July 23, 2023

Abstract

Proton aurora are the most commonly observed yet least studied type of aurora at Mars. In order to better understand the physics and driving processes of Martian proton aurora, we undertake a multi-model comparison campaign. We compare results from four different proton/hydrogen precipitation models with unique abilities to represent Martian proton aurora: Jolitz model (3-D Monte Carlo), Kallio model (3-D Monte Carlo), Bisikalo/Shematovich et al. model (1-D kinetic Monte Carlo), and Gronoff et al. model (1-D kinetic). This campaign is divided into two steps: an inter-model comparison and a data-model comparison. The inter-model comparison entails modeling five different representative cases using similar constraints in order to better understand the capabilities and limitations of each of the models. Through this step we find that the two primary variables affecting proton aurora are the incident solar wind particle flux and velocity. In the data-model comparison, we assess the robustness of each model based on its ability to reproduce a MAVEN/IUVS proton aurora observation. All models are able to effectively simulate the data. Variations in modeled intensity and peak altitude can be attributed to differences in model capabilities/solving techniques and input assumptions (e.g., cross sections, 3-D versus 1-D solvers, and implementation of the relevant physics and processes). The good match between the observations and multiple models gives a measure of confidence that the appropriate physical processes and their associated parameters have been correctly identified, and provides insight into the key physics that should be incorporated in future models.

Advancing Our Understanding of Martian Proton Aurora through a Coordinated Multi-Model Comparison Campaign

Andréa C. G. Hughes[1,2,3], Michael Chaffin[4], Edwin Mierkiewicz[3], Justin Deighan[4], Rebecca D. Jolitz[4], Esa Kallio[5], Guillaume Gronoff[6,7], Valery Shematovich[8], Dmitry Bisikalo[8,9], Jasper Halekas[10], Cyril Simon Wedlund[11], Nicholas Schneider[4], Birgit Ritter[12,13], Zachary Girazian[10], Sonal Jain[4], Jean-Claude Gérard[12], and Bradley Hegyi[6,7]

[1] NASA Goddard Space Flight Center, Greenbelt, MD, United States.

[2] Department of Physics & Astronomy, Howard University, Washington, DC, United States.

[3] Center for Space and Atmospheric Research (CSAR) and the Department of Physical Sciences, Embry-Riddle Aeronautical University, Daytona Beach, Florida, United States.

[4] Laboratory for Atmospheric and Space Physics, University of Colorado, Boulder, CO, USA. United States.

[5] Aalto University, School of Electrical Engineering, Department of Electronics and Nanoengineering, Espoo, Finland.

[6] NASA Langley Research Center, Hampton, VA, United States.

[7] Science Systems and Application Inc. Hampton, VA, United States.

[8] Institute of Astronomy of the Russian Academy of Sciences, Moscow, Russia.

[9] National Center for Physics and Mathematics, Russian Federation, Moscow, Russia.

[10] Department of Physics and Astronomy, University of Iowa, Iowa City, IA, United States.

[11] Space Research Institute, Austrian Academy of Sciences, Graz, Austria.

[12] Royal Observatory of Belgium, Brussels, Belgium.

[13] Université de Liège, LPAP – STAR Institute, Liege, Belgium.

Corresponding author (first): Andrea Hughes (Andrea.C.Hughes@NASA.gov)

Corresponding author (second): Michael Chaffin (Michael.Chaffin@colorado.edu)

Key Points:

- We undertake a multi-model comparison campaign to gain a better understanding of the physics and driving processes of Martian proton aurora
- The incident solar wind particle flux and velocity are found to be the two most influential parameters affecting the proton aurora profile

- The models effectively reproduce observations, with variations due to different model capabilities/solving techniques and input assumptions

Abstract

Proton aurora are the most commonly observed yet least studied type of aurora at Mars. In order to better understand the physics and driving processes of Martian proton aurora, we undertake a multi-model comparison campaign. We compare results from four different proton/hydrogen precipitation models with unique abilities to represent Martian proton aurora: Jolitz model (3-D Monte Carlo), Kallio model (3-D Monte Carlo), Bisikalo/Shematovich *et al.* model (1-D kinetic Monte Carlo), and Gronoff *et al.* model (1-D kinetic). This campaign is divided into two steps: an inter-model comparison and a data-model comparison. The inter-model comparison entails modeling five different representative cases using similar constraints in order to better understand the capabilities and limitations of each of the models. Through this step we find that the two primary variables affecting proton aurora are the incident solar wind particle flux and velocity. In the data-model comparison, we assess the robustness of each model based on its ability to reproduce a MAVEN/IUVS proton aurora observation. All models are able to effectively simulate the data. Variations in modeled intensity and peak altitude can be attributed to differences in model capabilities/solving techniques and input assumptions (*e.g.*, cross sections, 3-D versus 1-D solvers, and implementation of the relevant physics and processes). The good match between the observations and multiple models gives a measure of confidence that the appropriate physical processes and their associated parameters have been correctly identified, and provides insight into the key physics that should be incorporated in future models.

Plain Language Summary

The purpose of the present study is to gain a deeper understanding of the physics and driving processes of Martian proton aurora through a comparative modeling campaign. The models involved in this study have important similarities and differences, such as the dimensionality (*e.g.*, 3-D versus 1-D), inputs, and relevant physics included. We separate the modeling campaign into two steps: a first step comparing the models with each other (*i.e.*, model-model comparison), and a second step comparing the simulated model results with data from a proton aurora observation (*i.e.*, data-model comparison) taken by the Imaging UltraViolet Spectrograph (IUVS) onboard the Mars Atmosphere and Volatile EvolutioN (MAVEN) spacecraft. We find that all of the models are able to effectively simulate the data in terms of shape and brightness range of the proton aurora observation. The results of this study inform our understanding of the primary influencing factors that cause variability in the Martian proton aurora profile, the effects of dynamically changing solar wind parameters on the coupled Mars-Sun auroral system (*e.g.*, through extreme solar events such as coronal mass ejections and solar wind stream interactions), and the physical processes/constraints that should be considered in future modeling attempts of this unique phenomenon.

1. Introduction and Background

Proton aurora have been recently determined to be the most commonly observed type of aurora at Mars (Hughes *et al.*, 2019). This form of aurora is one of three primary types of Martian aurora, in addition to discrete (Bertaux *et al*., 2005) and diffuse aurora (Schneider *et al*., 2015). Further, even though this phenomenon was theoretically predicted by Kallio and Barabash (2001), proton aurora is the most recently discovered type of Martian aurora (Deighan *et al.*, 2018; Ritter *et al.*, 2018), and is thereby arguably one of the least studied and understood types of Martian aurora. Past efforts to model these phenomena have been unable to fully reproduce the observations (*e.g.,* Deighan *et al.,* 2018, in which the shape of the modeled profile resembled the data, but the modeled peak altitudes were consistently below the data and modeled intensities required adjustment via a scaling factor to match the data), suggesting a gap in our understanding and a need for further exploration of the underlying physics of these events through modeling.

Proton aurora can be identified in ultraviolet data as an enhancement in the hydrogen (H) Lyman-alpha (Ly-α) emission (121.6 nm) above the background coronal H brightness between an altitude of ~110-150 km; this enhancement is due to the contribution from the proton aurora-inducing H energetic neutral atoms (ENAs) as they collide with the atmosphere and emit photons (see Figure 1 from Hughes *et al*., 2019 for more detail and explanation of formation processes). In a previous statistical study, Hughes *et al*. (2019) used multiple Mars years of data from the Imaging UltraViolet Spectrograph (IUVS) (McClintock *et al*., 2015) onboard the Mars Atmosphere and Volatile EvolutioN (MAVEN) spacecraft (Jakosky *et al., 2015*) to assess the phenomenology of Martian proton aurora. Based on this study, they found that most Martian proton aurora events occur on the dayside of the planet (*i.e.*, at low solar zenith angles, SZAs) around the southern summer solstice (*i.e.*, solar longitude, L_s, ~270°). This seasonal increase in proton aurora activity was found to be correlated with the inflated Martian H corona around southern summer solstice, which corresponds with higher H column densities and H escape rates, caused by upper atmospheric temperatures and dust activity reaching an annual maximum during this time (*e.g.*, Hughes *et al*., 2019; Chaffin *et al*., 2021; Chaffin *et al*., 2014; Clarke *et al*., 2014; Halekas, 2017). This annual variability is also coupled with slightly higher solar wind proton fluxes as Mars is near perihelion (L_s = 251°). The seasonally increased abundance of H beyond the planet's bow shock during this season allows a larger fraction of solar wind protons to be converted into hydrogen ENAs (H-ENAs) (*i.e.*, through charge exchange), which can then bypass the bow shock and magnetic pileup boundary to create more frequent proton aurora events with very large Ly-α emission enhancements during this time of year.

The purpose of the present study is to gain a deeper understanding of the physics and driving processes of Martian proton aurora through a comparative modeling campaign. While previous data-driven statistical studies of these aurora provided an understanding of their phenomenology, frequency, and likely driving processes, much is still lacking in our knowledge. This includes, for example, the specific effects of variability in different input parameters on the shape, brightness, and peak altitude of the proton aurora profile, as well as the influence of model capabilities, solving techniques, and input assumptions on effectively simulating proton aurora observations. Modeling proton aurora activity provides an opportunity to understand these events, as it allows us to constrain different input parameters and predict variations in the results. Moreover, by undertaking a comparative modeling campaign in which the results of multiple models are evaluated (with each model emphasizing specific physical processes and utilizing different numerical solving techniques), we are able to simultaneously explore the range of

possible outcomes for individual auroral events. We note that the statistical study by Hughes *et al*. (2019) incorporated data from only the first ~two Mars years of MAVEN orbits, taken during the declining and minimum portion of the solar cycle. While the Hughes *et al*. (2019) study encompassed many proton aurora events, in this study we focus our efforts on modeling one specific event from the IUVS dataset that exhibited particularly interesting proton aurora activity.

Being able to effectively model Martian proton aurora is necessary for developing our understanding of observations of auroral events in the IUVS dataset, as well as the ability to predict and understand future observations. The purpose of this modeling campaign is not to determine which model is the "best" proton/hydrogen precipitation model in our study, but rather to identify the distinct capabilities each model provides in simulating proton/hydrogen precipitation at Mars. Through undertaking a rigorous assessment of Martian proton aurora using the results of multiple different simulations, we are able to develop an understanding of the gaps in our knowledge and improve our abilities to more effectively model future proton aurora observations.

2. **Modeling Campaign Description**

2.1. Campaign Outline/Steps

In order to accomplish the goals of this study, this campaign is divided into two primary steps: an inter-model comparison step (Step 1) and a data-model comparison step (Step 2). Each step is subdivided to reflect the "native format" (*i.e.*, original model outputs) and "forward-modeled" (*i.e.*, after running model outputs through radiative transfer model – described in more detail below) results (*i.e.*, Steps 1-A and 1-B, as well as Steps 2-A and 2-B). In the following sections we describe the models and discuss the results of each of these steps. We also consider the assumptions of each model and compare differences in the model capabilities (*e.g.*, the physics represented in each model) that may impact the results.

2.2. Models and Modeling Teams Involved in Campaign

In this study we utilize four different proton/hydrogen precipitation models and one radiative transfer model. Here we briefly discuss the different models and teams involved. Detailed descriptions of each of the four proton/hydrogen precipitation models used in the study and an overview table comparing their cross section assumptions are provided in supplementary material (Text S1-S4 and Table S1). A radiative transfer (RT) model is then used to "forward-model" the results of each step into observation space (*i.e.*, Steps 1-B and 2-B, respectively); this model is also briefly described below.

2.2.1. Proton/Hydrogen Precipitation Models

We include four unique proton/hydrogen precipitation models in this study: the Jolitz model (*i.e.*, "ASPEN"), the Kallio model, the Bisikalo/Shematovich *et al.* model, and the Gronoff *et al.* model (*i.e.*, "Aeroplanets"). The former three are Monte Carlo (MC) models (with the Jolitz and Kallio models being 3-dimensional (3-D) and the Bisikalo/Shematovich *et al.* model being 1-D). A MC simulation is a numerical technique that generates a range of possible outcomes and probabilities of occurrence for specific representative inputs. In such a simulation, a mathematical model is first constructed and then iteratively run using different random input

variables; the results can be considered in the context of a probability distribution curve and are averaged together to estimate the most likely outcome. In contrast, the Gronoff *et al.* model uses a 1-D Kinetic scheme, based on a semi-analytical treatment of the coupled H+/H Boltzmann kinetic transport equation.

2.2.1.1. Jolitz 3-D Monte Carlo model ("ASPEN")

The Jolitz model, *i.e.*, ASPEN (Atmospheric Scattering of Protons, Electrons, and Neutrals), is a 3-D Monte Carlo test particle simulation. This model was initially developed to predict atmospheric ionization rates at Mars by solar energetic particles, which have higher energies than the ENAs studied in this paper (Jolitz *et al.*, 2017), and has since been used to predict precipitating SEP electron fluxes at Mars (Jolitz *et al.*, 2021). The model solves the Lorentz force equations for energetic particle motion and uses a Monte Carlo approach to predict collisions and resulting energy loss in the atmosphere.

Using ASPEN, stochastic collisions are modeled by inverting the relation between intensity, density, and absorption cross section for a particle beam incident on a medium of scatterers (colloquially known as Beer's law) to dynamically calculate a probability distribution function that is combined with a random number to predict variable distances between collisions. This probability distribution function is calculated for each individual particle and depends on the position, path, and energy through the planetary atmosphere. Similarly, whenever a collision occurs, the type of collision is predicted probabilistically using the relative cross section of each possible collisional process and the particle energy is decremented by the corresponding energy loss. As a particle loses energy, the relative cross sections of each process change.

This model (as well as all models in this study) is highly dependent on the choice of cross sections. For the application in this study, the selected cross sections for hydrogen and proton impact on carbon dioxide are described in Jolitz *et al.* (2017), with one exception: the cross sections for proton- and hydrogen-impact excitation was replaced with Ly-α emission cross sections. ASPEN uses a cross section calculated by scaling the corresponding emission cross sections from impact on molecular oxygen.

Since ASPEN is a 3-D Monte Carlo simulation, predicting an accurate emission rate requires appropriate choice of initial conditions and a large volume of simulated particles. For Step 1, we simulate 10,000 particles incident on the subsolar point from an altitude of 600 km and calculated the emission rate by binning all Ly-α emitting collisions as a function of altitude and multiplying by the incident flux. For Step 2, we simulate 10,000 particles uniformly distributed in space on a plane perpendicular to the direction of solar wind flow. Each particle represents a fraction of the assumed incident flux. The emission rate was then calculated by weighing the total number of emissions binned by altitude, solar zenith angle, and the fraction of flux associated with each simulated particle.

2.2.1.2. Kallio 3-D Monte Carlo model

The Kallio model is a 3-D Monte Carlo model where the incident particle, either H^+ or H, collides with neutral particles, after which the velocity of the particle is changed. The model includes 6 elastic and 24 inelastic processes; however, in this study, only the processes mentioned in the main text of this paper were used.

The model inputs are neutral atom densities, energy dependent total cross sections, the differential scattering cross sections (DSCS), the number of precipitating particles (5,000 particles in the Step 1 runs and 100,000 particles in Step 2 runs), and the initial positions and velocities of the precipitating particles (in the present case hydrogen atoms). The total cross sections are given in Kallio and Barabash (2001, Table 1 and Fig. 3) and the DSCS scattering angle distribution in Kallio and Barabash (2000, Fig. 1, "nominal") and Kallio and Barabash (2001, Fig. 2). Total cross sections give the probability that a collision occurs. Random numbers are used to model if a collision occurs, and which collision process occurs. If a collision happens, then the DSCS determines the new velocity of the incident particle after collision. The value of the scattering angle is obtained by using a new random variable.

The largest uncertainty for the obtained Ly-α volume emission rate is related to the uncertainty of the total cross sections used and the DSCS between H and H^+ particles and CO_2 molecules. In the simulation many of these H/H^+ collisions with CO_2 are modeled with H/H^+ collisions with O_2 and N_2 which was published in the literature (see Kallio and Barabash, 2001, Table 1, for details).

In the simulation, particles are injected into the upper atmosphere at the point [x, y, z] = [260 km + R_{Mars}, 0, 0], where the radius of Mars, R_{Mars}, is 3393 km. The model saves the position and the velocity of the particle if it has a Ly-α collision process. The Ly-α volume production rate was derived from the saved positions of Ly-α processes by collecting the number of the Ly-α collision processes at a given altitude range. Then the Ly-α volume emission was derived by using a 1-D approximation, *i.e.*, assuming that the area of the emission perpendicular to the x-axis is equal to the initial area in the solar wind through which the precipitating particles initially came. In the plots presented in this paper the Ly-α emission altitude profiles were derived in 1 km altitude bins.

2.2.1.3. Bisikalo/Shematovich et al. 1-D Monte Carlo model

The Bisikalo/Shematovich *et al*. model is a 1-D Monte Carlo model. The model considers three primary processes: 1) precipitation of high-energy hydrogen atoms and protons that lose their kinetic energy in the elastic and inelastic collisions, 2) ionization of target atmospheric molecules/atoms, and 3) charge transfer and electron capture collisions with the major atmospheric constituents (*i.e.*, CO_2, N_2, and O). Secondary fast hydrogen atoms and protons carry enough kinetic energy to cycle through the collisional channels mentioned above and result in a growing set of translationally and internally excited atmospheric atoms and/or molecules.

To study the precipitation of high-energy H/H^+ flux into the planetary atmosphere, we use the kinetic Monte Carlo model to solve the kinetic Boltzmann equations (Shematovich *et al*., 2011; Gérard *et al*., 2000) for H^+ and H. The model is 1-D in geometric space and 3-D in velocity space. Nevertheless, the 3-D trajectories of H/H^+ are calculated in the code with final projection on radial direction. The current version of the MC model (Shematovich *et al*., 2019) incorporates the full structure of the induced magnetic field of Mars; that is, all three components of the magnetic field $\mathbf{B} = \{Bx,By,Bz\}$ are taken into account. The details of the model implementation and statistics control with the variance below 10% can be found in Shematovich *et al.* (2019).

The essence of the kinetic Monte Carlo model is accounting of all possible collisions in the atmospheric region studied. Therefore, statistics for all collisional processes are accumulated

during the numerical realization of the kinetic model of the proton aurora. It provides a good basis for the evaluation of the Ly-α source functions as keeping all excitation processes and their spatial characteristics makes it possible to determine the statistical distribution of the emitted Ly-α photons.

A key aspect of this model is the probabilistic treatment of the scattering angle distribution, which influences both the energy degradation rate and the angular redistribution of the precipitating protons and hydrogen atoms (Bisikalo *et al*., 2018; Shematovich *et al*., 2019). The model utilizes both total and differential cross sections when calculating the post-collision velocities for high-energy precipitating H/H^+ and atmospheric particles.

The region under study is limited by the lower boundary, which is placed at 80 km, where H/H^+ particles are efficiently thermalized. The upper boundary is set at 500 km, where measurements or calculations of the precipitating fluxes of protons or hydrogen atoms are used as a boundary condition. Both table and/or analytic (Maxwellian and/or kappa-distribution) functions representing the energy spectra as well as the pitch-angle (monodirectional, isotropic, or limited by cone) distributions of precipitating particles could be used at the upper boundary.

2.2.1.4. Gronoff et al. 1-D Kinetic model ("Aeroplanets")

The Gronoff *et al.* model, called Aeroplanets, utilizes a 1-D Kinetic transport approach. Aeroplanets (Gronoff *et al*., 2012a; Gronoff *et al*., 2012b; Simon Wedlund *et al.,* 2011) is based on an auroral particle precipitation model initially developed for the Earth and later adapted to Mars (as well as numerous other planetary bodies, *e.g.*, Venus and Titan). This model computes the ionization and excitation of atmospheric species by photon, electron, proton, and cosmic ray impacts, including the effect of secondary particles. The proton transport module within Aeroplanets is based on the work of Galand *et al.* (1997 and 1998), Simon (2006), and Simon *et al.* (2007) for Earth, who solved semi-analytically the coupled proton-hydrogen dissipative kinetic transport equation for protons and hydrogen atoms charge-changing with neutral gas. It was originally developed from the idea that dissipative forces responsible for angular redistributions (due to elastic scattering) can be introduced in the force term of the general dissipative Boltzmann equation (Galand *et al*., 1997). As such, angular redistributions due to magnetic mirroring effects and to collisions are naturally included, leading to backscattering.

Inputs to the Aeroplanets model include cross sections, the vertical profile of atmospheric neutral densities (*i.e.*, composition at different altitudes), and the precipitating fluxes of particles such as H and H^+ at the top of the atmosphere (any shape and energy distribution can be prescribed). Outputs include the vertical profile of H and H^+ differential energy fluxes, and the vertical profile of the production rate of excited and ionized species and electrons, including emissions. Simulations are performed on a grid typically spanning 90 to 250 km (approximately, the exobase level).

Cross sections in Aeroplanets are taken from the latest version of the ATMOCIAD (Gronoff *et al.*, 2021) cross section and reaction rate database compiled and developed by Simon Wedlund *et al*. (2011) and Gronoff *et al*. (2012a). In ATMOCIAD, experimental and theoretical cross sections as well as their uncertainties are collected. Although ATMOCIAD is an extensive collection of cross sections, we note that there is still a rather poor characterization of cross sections at low energies (typically in the sub-keV range). Regarding differential cross sections, Aeroplanets uses phase functions that are convolved with the energy-dependent cross sections described above.

Aeroplanets is well qualified for the fast computation of the proton precipitation from a measured spectra near the planet, and for the fast computation of the whole effect of that precipitation thanks to its coupling with a secondary electron transport model. The analytic computation approach prevents the computation within very complex magnetic topologies (which are best handled by Monte-Carlo models) but is suited for handling large sets of initial angles and energies.

2.2.2. Radiative Transfer Model

To quantitatively compare the proton aurora modeling results and the IUVS limb observations it is necessary to perform a radiative transport calculation (done in this study using a Radiative Transfer model created by coauthor Deighan). While the Ly-α emission from thermal hydrogen is optically thick in the upper atmosphere of Mars (Anderson and Hord, 1971), the emission associated with proton aurora can be considered optically thin due the large Doppler shifting caused by the high velocity of the ENAs (Gérard et al., 2019). This both offsets the line center and broadens the width of the spectral line shape and ensures that few of the photons produced by proton aurora interact with the ambient thermal hydrogen population for most viewing geometries. This allows a simple line-of-sight integration to be employed, though CO_2 absorption must still be taken into account (Deighan *et al.*, 2018; Gérard *et al*., 2019).

The procedure used to calculate a model brightness to compare with each measurement by IUVS is as follows: First, the model atmosphere is sampled at 1 km intervals starting from the reconstructed spacecraft position and extending out 3000 km along the line-of-sight vector. This ensures adequate sampling of the model volume emission rate (VER), as the auroral emission typically has a scale height on the order of 10 km and a peak VER occurring 500-1700 km away from the spacecraft for IUVS periapsis limb scans. The column of CO_2 between the spacecraft and each sample point in the model is then integrated and an absorption optical depth is obtained using an absorption cross section of 7.348×10^{-20} cm^2 (Huestis and Berkowitz, 2010). The Beer-Lambert law is then applied to find the attenuation caused by CO_2 absorption for each sample point and the attenuated VER is integrated to obtain a column emission rate (CER). This is readily converted into the brightness unit of Rayleighs (R) conventionally used for airglow and aurora (Hunten *et al.*, 1956). The proton aurora VER and CO_2 densities are both assumed to have spherical symmetry (primarily driven by the use of 1-D profiles), and the brightness calculation itself is performed using an integration through 3-D space along each line of sight.

3. **Inputs and Results for Inter-model Comparison (Step 1)**

3.1. Purpose and Description of Step 1

We begin the campaign with an inter-model comparison in Step 1 using multiple different test cases of representative inputs to represent varying proton aurora conditions. The purpose of this step is to set a baseline for inter-model comparisons, and to compare the effects of varying input conditions on the results of each individual model.

We use five different representative proton aurora conditions, each with varying solar wind velocity, H-ENA and proton fluxes at the top of the atmosphere, and CO_2 density profiles for high and low atmospheric temperature conditions (Table 1). Using these inputs, altitude versus Ly-α volume emission rate profiles were created by each model for each representative test case. In Step 1-A, we first compare the results in each modeler's native format (*e.g.*, volume

emission rate). In Step 1-B the results are forward-modeled into observation space using the radiative transfer model. In Section 5 we discuss possible causes for the observed inter-model discrepancies.

3.2. Assumptions/Constraints for Step 1

To accurately compare the driving physics incorporated in each of the models, we implement a number of constraints on each model in Step 1 (*i.e.,* the inter-model comparison step). The three primary constraints are 1) assuming the incident solar wind particle beam (either purely H or purely H+) is monoenergetic; 2) assuming purely 1-D anti-sunward solar wind particle movement (*i.e.,* monodirectional) incident at the subsolar point (*i.e.,* SZA = 0°); and 3) requiring that the same cross section processes be included in each model (yet allowing the use of different cross section values; see Section 5.1 and Supplementary Table S1 for more details). We empirically justify inclusion of the first two constraints based on previous observations of penetrating protons showing a monoenergetic population (*i.e.*, typically the same energy as the solar wind) that is incident across the entire sunward-facing side of the planet (*e.g.,* Halekas *et al*., 2015). For the third constraint, we specifically consider five cross section processes for protons and/or H interacting with CO_2: elastic, charge exchange/electron capture, electron stripping, ionization, and Ly-α. Although all models have the ability to incorporate additional processes (see Supplementary Table S1), most have incorporated exclusively these five processes. We note that the Bisikalo/Shematovich *et al*. team also included cross section processes for Hydrogen Balmer-alpha and -beta; however, this inclusion produces only a very minor effect on the resulting volume emission rate (VER) due to the relatively small cross sections of these processes. Each modeling team also incorporated their own DSCS values (Supplementary Table S1). Lastly, while the Jolitz and Kallio models use similar 1 km linear altitude bins, the other two models utilize different types of altitude binning (we note however, that a comparison of the type and spatial resolution of the altitude bins used by the Gronoff *et al*. model found that this parameter to have a negligible effect on the simulation results).

3.3. Representative inputs for Step 1

In undertaking the inter-model comparison, we create five representative proton aurora events to be simulated by each model (Table 1). We select baseline cases that resemble previous observations of the particle flux, velocity, and neutral CO_2 temperature of Martian proton aurora (*e.g.*, Deighan *et al*., 2018), and incrementally change the input parameters in each case in order to quantify the effect of the parameters on the proton aurora profile. In the two baseline cases we vary the type of incident particle at the top of the model atmosphere (*i.e.,* 100% H-ENAs or 100% protons in Case 1 and Case 2, respectively); in subsequent cases we vary the average incident particle beam flux (Case 3), the particle velocity (Case 4), and the neutral atmospheric temperature (Case 5). By changing the temperature in Case 5, we also modify the scale height, and thereby the CO_2 density profile. In Step 1 we do not include any representative cases that consider variability associated with magnetic fields or solar zenith angles (SZAs) (*i.e.*, the models simulate particle incidence at the subsolar point, where the Ly-α intensities are highest on the planet). While these constraints are not necessarily indicative of the actual Mars-solar wind interactions, they represent simplified scenarios that are beneficial for gauging inter-model variability. We note that in this study we are exclusively interested in modeling the proton aurora profile under different input conditions; since proton aurora are almost entirely formed due to interactions between the incident particles and the neutral CO_2 atmosphere, the model results do

not directly incorporate processes occurring in the extended corona upstream of the bow shock (*e.g.*, charge exchange between solar wind protons and the H corona; however, all but Case 2 implicitly include this process).

Table 1: Representative input for the five example cases in the inter-model comparison step (Step 1). These parameters were varied to assess their relative importance in each model.

	Case 1 (Baseline w/ H-ENAs)	Case 2 (Baseline w/ Protons)	Case 3 (Small Flux)	Case 4 (High Velocity)	Case 5 (Hot Atmosphere)
v [km/s]	400	400	400	800	400
$F_{H\text{-}ENA}$ [$cm^{-2}s^{-1}$]	10^7	0	10^6	10^7	10^7
F_{proton} [$cm^{-2}s^{-1}$]	0	10^7	0	0	0
CO_2 Density Profile (varying Temp)	CO_2 profile @ T=190K	CO_2 profile @ T=190K	CO_2 profile @ T=190K	CO_2 profile @ T=190K	CO_2 profile @ T=240K

In order to vary the neutral atmospheric temperature parameter in the models (Case 5) we create two different CO_2 density profiles, each containing altitude-binned (1 km bin) representative CO_2 number density values for the two respective temperature ranges of 190 K (*i.e.*, baseline temperature) and 240 K (*i.e.*, high temperature). These different CO_2 density values were created using a standard barometric isothermal atmosphere described by the equation:

$$n(z) = n_{ref} \exp\left(- (z - z_{ref}) / H \right), \quad (1)$$

where z is altitude, n_{ref} is the number density at a reference altitude, z_{ref} is the chosen reference altitude (in this case, 120 km), and H is the CO_2 scale height. Here we assume $n_{ref} = 1 \times 10^{11}$ cm^{-3} at 120 km, and H is calculated for each temperature range using a value of g = 3.46 m/s^2 (*i.e.*, g at the reference altitude of 120 km). The calculated scale height values for the low and high temperature cases were 10.4 km and 13.1 km, respectively.

3.4. Results of Step 1-A

The results of the inter-model comparison in Figure 1 show many similarities between the different modeled proton aurora volume emission rates (VERs), with the results of the Jolitz and Kallio models exhibiting the most similarities. Interestingly, most models predict similar trends in the relative changes observed between each of the five representative cases. There is a large range in the proton aurora peak altitudes between the models, with the Bisikalo/Shematovich *et al.* model consistently predicting the lowest peak altitudes and the Gronoff *et al.* model predicting the second lowest. The peak altitudes in the Jolitz and Kallio models are consistent with each other in nearly every case, with the exception of the high velocity case (Case 4), where the Jolitz model predicts a slightly lower peak altitude than the

Kallio model. The Gronoff *et al.* model also consistently predicts the largest peak VERs in each case (with the exception of Case 2, where the Bisikalo/Shematovich *et al.* model predicts the largest peak VERs). Almost all of the models show no difference in the proton aurora profile (*i.e.*, VER or altitude) based on varying the type of incident particle at the top of the atmosphere (*i.e.*, H-ENA or proton; compare Case 1 and Case 2 profiles); the only exception being the Bisikalo/Shematovich *et al.* model, which predicts a slight increase in the VER of the proton aurora profile for protons rather than H-ENAs as the incident particle. The similarities between Cases 1 and 2 suggest that most models do not predict significant differences between a H-induced Ly-α emission and a proton-induced Ly-α emission in the proton aurora profile.

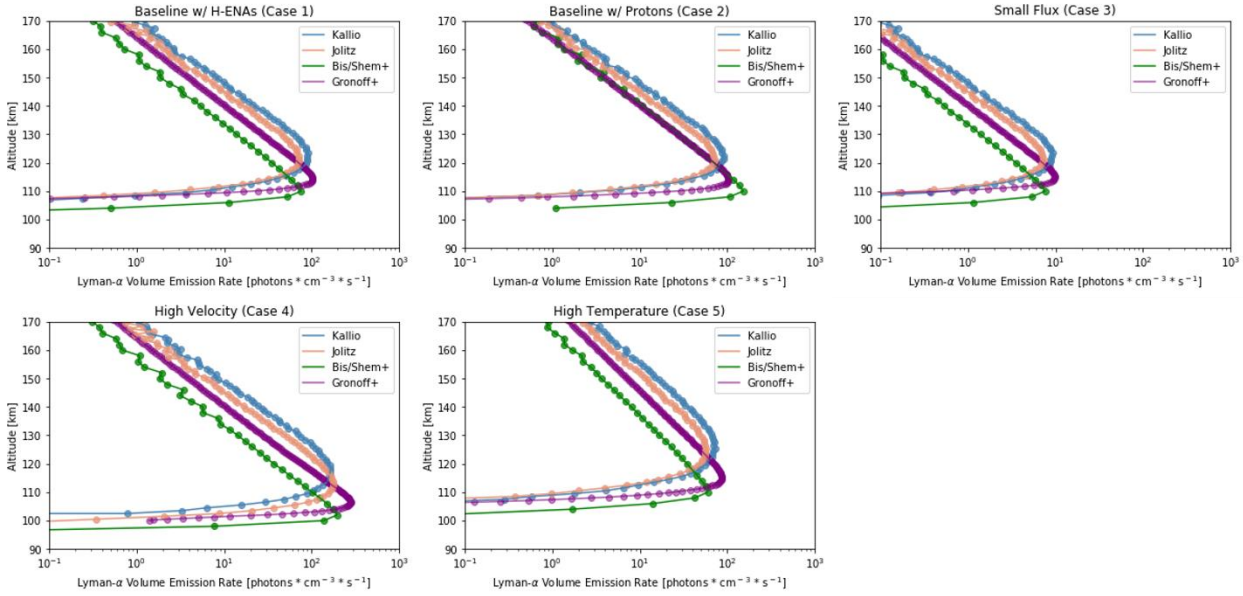

Figure 1: Simulated Ly-α volume emission rates of proton aurora at different altitudes from each model in this study for the five representative input cases in the inter-model comparison step of the campaign (Step 1-A). The two input parameters that have the most significant effect on the results are the incident solar wind flux and velocity. See Table 1 for the input parameters used in each of the five representative cases.

3.5. Results of Step 1-B

In Step 1-B we forward-model the results of Step 1-A into observation space (*e.g.*, perform a "line-of-sight" integration comparison). In this step we produce synthetic observations that would be made by MAVEN/IUVS given the computed volume emission rates. In so doing, the model results are converted from Ly-α volume emission rate (in units of photons/cm^{3}s) to Ly-α intensity (in units of kilorayleighs, kR) using the previously described radiative transfer model. Using the same radiative transfer model to forward-model each simulation's output in this step enables a more reliable cross-model comparison.

As shown in Figure 2, the results of Step 1-B further reveal similarities in the model intensities and peak altitudes for each of the five cases. We find consistently in each model that the two major variables that affect the proton aurora profile are the penetrating particle flux and the particle velocity. Decreasing the flux by an order of magnitude (Case 3) correspondingly decreases the Ly-α intensity by an order of magnitude. Similarly, doubling the particle velocity (Case 4) noticeably increases the peak intensity in each model and decreases the peak altitude by ~5-10 km. In the final representative input case of increasing the atmospheric temperature

(thereby changing the neutral atmospheric scale height) (Case 5), all of the models show a slight decrease in the Ly-α peak intensity and a change in the shape of the profile at higher altitudes (*i.e.*, the profile has a broader shape). Additionally, most of the models show an increase in the peak altitude by ~1-5 km in Case 5 (with the exception of the Bisikalo/Shematovich *et al.* model, which does not exhibit a change in the peak altitude due to the changing temperature/scale height). The differences in the profile observed in Case 5 are likely present because the volume emission rate, and therefore the unattenuated auroral brightness, scales inversely with the atmospheric scale height in order to conserve photon production in the atmosphere; this in turn causes the Ly-α brightness to appear more "spread out" across different altitudes in the proton aurora profile.

The consistency of these results between models confirms our understanding of the driving processes that have the most significant effect on the proton aurora profile. Particularly, we see in Cases 3 and 4 that the solar wind proton velocity and density (which also affect the particle energy and flux) are tremendously important in the formation of notable proton aurora events. Thus, we may extrapolate from the results that high velocity and/or density solar events (*e.g.*, coronal mass ejections and corotating interaction regions) will correspondingly create significantly enhanced proton aurora events. This finding is consistent with preliminary studies of proton aurora at Mars in which the observations were found to correspond with extreme solar activity events (*e.g.*, Ritter et al., 2018).

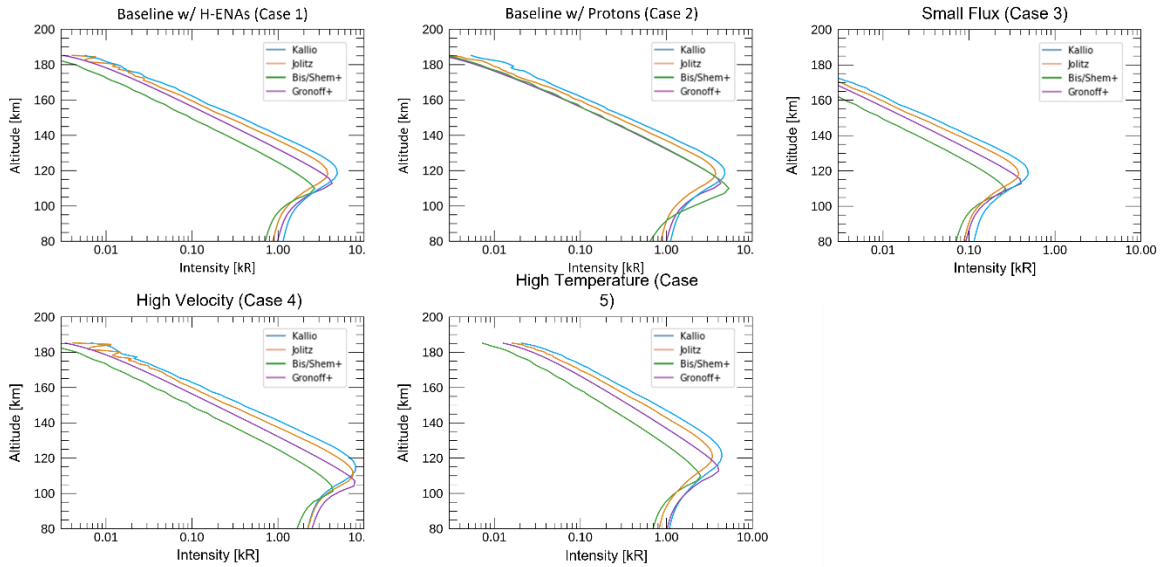

Figure 2: Simulated Ly-α intensities from the inter-model comparison after running the results of Step 1-A through the radiative transfer (RT) model (Step 1-B), which forward-models the results into observation space (e.g., performs a "line-of-sight" integration comparison). The model results more closely resemble each other after this step, but the dominant influencing factors identified in Step 1-A (Figure 1) are still present. See Table 1 for the input parameters used in each of the five representative cases.

4. Inputs and Results for Data-Model comparison (Step 2)

4.1. Purpose and Description of Step 2

In the second step, we assess the robustness of each of the models based on their abilities to reproduce a typical proton aurora detection from the MAVEN/IUVS dataset. In undertaking

Step 2, different variables in the models were tuned to match proton aurora events in the MAVEN/IUVS dataset. The models use relevant data inputs for a specific proton aurora event to attempt to accurately reproduce the event. As in Step 1, the model results in Step 2-A are first provided in their native formats, and subsequently forward-modeled into observation space in Step 2-B using the radiative transfer model.

4.2. Description of Example Proton Aurora Event and MAVEN/IUVS Observations

For the data-model comparison stage of the campaign (Step 2), we selected an example of a proton aurora event from the MAVEN/IUVS dataset that occurred during the periapsis portion of MAVEN orbit #4235 (*i.e.*, December 3rd, 2016, starting at ~13:44 UTC). This particular proton aurora event occurred at relatively low SZAs around southern summer solstice (L_s ~270°), a period of time exhibiting frequent proton aurora activity and increased dust activity associated with the concurrent Martian dust storm season. Figure 3 shows the IUVS Ly-α intensity data for this orbit. The left-hand plot of Figure 3 shows the Level 1C altitude-binned Ly-α altitude-intensity profiles for each of the limb scans used in the study; and the right-hand plot shows these profiles overlain on a synthetic image format of each of the IUVS limb scans from this orbit (horizontal), showing the Ly-α intensity for each of the 21 IUVS mirror integrations (vertical) and 7 spatial bins within each scan (*e.g.*, similar to Figure 2 in Deighan *et al*., 2018). Note that the scans are displayed as though they are contiguous even though spacecraft and slit motions prevent full spatial coverage. There are eleven IUVS limb scans in this orbit, but we use only the middle nine IUVS scans in this study (yellow highlighted scans in Figure 3). In evaluating the robustness of each of the models in this step of the study, the model results were compared with intensities and peak altitudes of the IUVS Ly-α profiles from these nine scans.

There are minor peak altitude variations in IUVS Ly-α observations between scans throughout this orbit. These minor altitude variations correspond with similar altitude variations in the IUVS CO_2^+ ultraviolet doublet emission (CO_2+ B $2\Sigma \rightarrow$ X 2Σ around 288 nm) (not shown), suggesting the possible presence of waves and/or tides in the neutral atmosphere during this orbit (*e.g.*, Lo *et al*., 2015; England *et al.*, 2016). The likely presence of waves/tides in this orbit is strengthened by similar observations in the MAVEN/NGIMS inbound CO_2 altitude-density profile. We note, however, that altitude variations in the Ly-α and CO_2^+ emissions are less than 5 km, approaching the resolution limit of the observation; thus, the minor altitude variations observed in the Ly-α peak intensity or CO_2 density during this orbit should not have any significant influence on the modeled proton aurora profiles.

This particular proton aurora event exhibits an especially high orbit-mean Ly-α peak intensity and emission enhancement (11.4 and 3.93 kR, respectively) as observed by IUVS. Also notable during this orbit is a particularly high penetrating proton flux (2.73×10^6 cm^{-2} s^{-1}) observed by MAVEN's Solar Wind Ion Analyzer (SWIA) instrument (Halekas *et al.*, 2013). SWIA observed a strong solar wind stream interaction during this orbit, resulting in this especially high penetrating proton flux. The MAVEN periapsis during this orbit was in the southern hemisphere on the dayside of the planet (with the exception of a few limb scan observations near the terminator) (see Supplementary Figure S1 and Figure S2). Because the spacecraft periapsis does not occur near any remanent crustal fields (Supplementary Figure S1), we do not expect a significant influence (if any) from crustal fields during these observations.

The average upstream interplanetary magnetic field (IMF) magnitude and cone angle (*i.e.*, angle off of the Mars-Sun line) during this orbit is ~10 nT and ~45°, respectively.

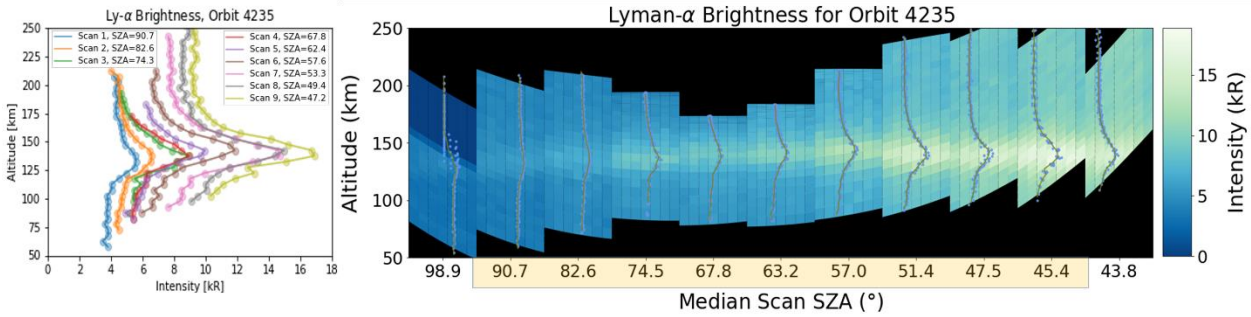

Figure 3: IUVS Ly-α intensity data of proton aurora observation used in the data-model portion of the campaign (Step 2). ***Left****: IUVS Level 1C altitude-intensity profiles for limb scans used in the study (MAVEN orbit #4235); SZA at the profile peak for each limb scan is shown in the legend.* ***Right****: Altitude-intensity profiles overlain on top of a synthetic image format of Ly-α intensities for each IUVS limb scan/mirror angle in this orbit (e.g., similar to Figure 2 from Deighan et al. 2018; see text for more details). Note that the scans are displayed as though they are contiguous but spacecraft and slit motions prevent full coverage. Only the central nine scans are used in this study (scans that are highlighted yellow at the bottom), and the SZA values shown at the bottom correspond with the median SZA for each limb scan in the orbit.*

4.3. Background Subtraction of Coronal H Contribution from IUVS Ly-α Brightness

The Ly-α brightness observed in the IUVS data is created by contributions from not only the non-thermal solar wind-derived H that produces proton aurora, but also from the thermalized background coronal H. Thus, by subtracting out the background coronal H from the IUVS proton aurora profiles, we are able to accurately compare the data with the model results. We perform this coronal H background subtraction by first estimating the background coronal H brightness during this time using IUVS limb scan profiles from a nearby orbit that exhibits little/less evidence of enhancement due to proton aurora activity at a similar SZA (in this case we use orbit #4229, as it exhibits the least contribution from proton aurora than any surrounding orbits). These heuristic coronal Ly-α profiles are created by fitting an arcsine function to the upper- and lower-most altitudes of the Ly-α profiles from the nearby orbit with little/less proton aurora activity. Each heuristic profile of the estimated background Ly-α brightness due to the coronal H in a given orbit is then subtracted out from each corresponding IUVS limb scan at a similar SZA from the orbit of interest containing strong evidence of proton aurora (see Supplementary Figure S3 for Ly-α profiles before and after background subtraction and heuristic coronal background profiles used). This method is similar to the background subtraction methodology used by Deighan *et al.* (2018) but differs in the determination of the background coronal H profile due the absence of nearby orbits that completely lack proton aurora (*i.e.*, because of the before mentioned near continuous proton aurora activity during the southern summer season). The corrected intensities should then more closely reflect the H Ly-α contribution only from proton aurora. In order to determine its effectiveness, this background coronal H subtraction technique was tested on numerous other IUVS proton aurora detections and found to be a highly effective empirical method for isolating the proton aurora contribution to the IUVS Ly-α observations. However, as this methodology estimates a heuristic background coronal H by assuming minimal/no changes in the neutral atmosphere between multiple orbits, there will be inaccuracies in the corrected proton aurora profiles; we estimate these inaccuracies to be only a fraction of a kR at most.

As shown in Supplementary Figure S3, the IUVS Ly-α intensities are reduced significantly due to this background-subtraction routine (by nearly 10 kR at low SZAs), but the shape of the profiles around the proton aurora profile peak (*i.e.*, between ~110-150 km) does not change. The profile peak altitudes typically also do not change as a result of this background subtraction methodology, provided that the peak altitudes of the proton aurora orbit profiles are not significantly different from those of the background subtraction orbit profiles (*i.e.*, the nearby orbit with little/less enhancement due to proton aurora). However, because of a slight difference in peak altitudes between the orbit considered in this study and the orbit used for the background subtraction routine (*i.e.*, orbits 4235 and 4229, respectively) at the lowest SZA profile, the peak altitude of the SZA ~45° background subtracted profile has been (artificially) slightly shifted down by ~5 km.

4.4. Assumptions/Constraints for Step 2

In Step 2, the models used inputs drawn from observations made by MAVEN (discussed more below). We apply many of the same constraints and assumptions as those applied in Step 1 (*i.e.*, assuming a monoenergetic incident particle beam and monodirectional incident particle movement, and constraining the cross section processes used). One notable difference in Step 2 is that the models produced outputs at a range of solar zenith angles (*i.e.*, not just at the subsolar point) in order to simulate the different SZAs of each of the IUVS limb scans in this orbit. As in Step 1, we exclude any effects due to electric or magnetic fields.

In order to additionally simplify the inputs for this step, all models assume that the incident particle population is composed entirely of H-ENAs at the top of the atmosphere (*i.e.*, assuming an initial penetrating proton component equal to zero). Based on our findings in Step 1, the proton aurora profile does not significantly change in most models when assuming 100% protons or 100% H-ENAs. Thus, this assumption of particle composition should not significantly affect the final results. The initial H-ENA flux ($F_{H\text{-}ENA}$) is approximated using the equation:

$$F_{H\text{-}ENA} = F_{pp} \times 13.5, \quad (2)$$

where F_{pp} (the orbit mean penetrating proton flux derived from SWIA) equals 2.73×10^6 cm^{-2} s^{-1} in this orbit, and 1/13.5 is the approximate fraction of the incoming beam of H-ENAs that is converted to protons. This conversion value was determined based on previous SWIA observations and the relevant energy-dependent electron stripping and charge exchange cross sections (*e.g.*, Halekas *et al.*, 2015; Halekas, 2017), assuming that at the point when $H\text{-}H^+$ equilibrium is reached in the collisional atmosphere (*i.e.*, the location of the SWIA measurement) the mix is ~92.5% ENAs and ~7.5% protons (*i.e.*, the equilibrium fractionation for the relevant cross sections at 1 keV).

Another constraint carried over from Step 1 is that all models used the same representative CO_2 density (*i.e.*, a 1 km altitude-binned CO_2 number density profile). However, in Step 2, the theoretical CO_2 density line profile is created based on neutral densities from two MAVEN instruments observing at different altitude ranges during this orbit: IUVS and the Neutral Gas and Ion Mass Spectrometer (NGIMS) (Mahaffy *et al.*, 2015). We note that although NGIMS data are acquired during both the inbound and outbound portions of the orbit, we restrict this study to include only inbound data, due to instrument artifacts which have been found to artificially increase CO_2 densities in NGIMS outbound data (*e.g.*, Stone *et al.*, 2018). The IUVS and NGIMS neutral densities are consistent with each other within the limited overlapping altitude range of the two instruments (*i.e.*, at a reference altitude of 170 km, the NGIMS CO_2

density is ~1.48×10^{9} cm^{-3}, and the smallest derived CO_2 density from different IUVS limb scans is ~1.74×10^{9} cm^{-3}).

Figure 4 shows the theoretical CO_2 profile for Step 2, which is created by fitting an exponential to the IUVS and inbound NGIMS data using equation (1). In this case, n_{ref} = 1.1×10^{11} cm^{-3} (the average IUVS density at reference altitude z_{ref}), z_{ref} = 130 km (the minimum altitude observed by IUVS during this orbit). The CO_2 scale height was estimated by varying the temperature value until an appropriate fit was achieved (using a value of g = 3.41 m/s^2 at 130 km); a temperature of 180 K was found for the best-fit line.

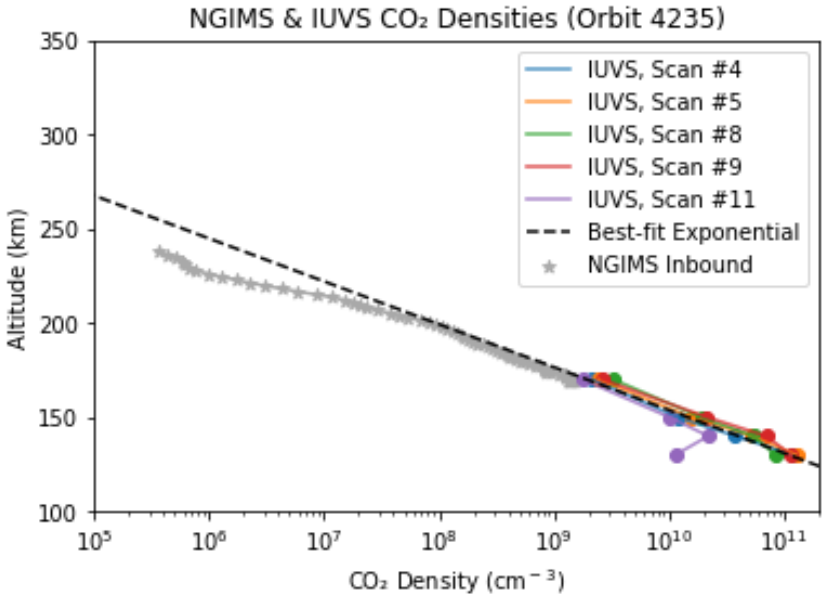

Figure 4: Empirically-derived theoretical CO_2 profile used by models for the data-model comparison (Step 2). This profile was created by fitting a best-fit exponential to the derived IUVS and measured NGIMS inbound data from this MAVEN orbit.

4.5. Results of Step 2-A

The results of Step 2-A show that all models simulate the input data to within less than an order of magnitude of the same volume emission rates (VERs) (Figure 5). As in Step 1, the results of Step 2-A also show that the Jolitz and Kallio simulations exhibit the most similarities to each other in terms of VERs and peak altitudes. The Gronoff *et al*. model results exhibit relatively low VERs compared with other models.

In Step 1, we used the models to simulate a proton aurora profile at a single SZA (*i.e.*, the subsolar point). However, in Step 2, each model simulated proton aurora profiles at numerous SZAs between ~45°-90°. Thus, in Step 2 we are able to observe the decrease in Ly-α proton aurora brightness associated with increasing SZA. The proton aurora brightness appears to monotonically decrease in the Kallio, Jolitz, and Gronoff *et al*. simulations (particularly at low SZAs), but in the Bisikalo/Shematovich *et al.* simulation results the decrease is more gradual at lower SZAs (and pronounced at higher SZAs).

We note that the Bisikalo/Shematovich *et al.* Monte Carlo calculations for the two highest SZA profiles (*i.e.*, SZA=82.6° and 90.7°) resulted in practically no Ly-α excitations (hence their absence on the plots in Figure 5 and Figure 6). The Bisikalo/Shematovich *et al.*

model results also exhibit relatively low peak altitudes at lower SZAs in comparison with other models; however, this model is the only one showing variability in the peak altitudes between SZA profiles. In this 1-D kinetic model, Ly-α photons are excited in local collisions of H-ENAs with the ambient atmospheric gas and the VERs are accumulated for the projection velocities of H-ENAs into the given SZA direction. In the case of high SZAs, the Ly-α excitations are caused mainly by the H-ENAs moving in the tangential trajectories relative to the upper atmosphere (*i.e.*, by H-ENAs which do not penetrate deep into the atmosphere). This results in: a) very low values of Ly-α VERs for high SZAs (especially for runs with SZA=82.6° and 90.7°); and b) an increase of the peak height of the profiles with SZA (*i.e.*, because the kinetic energy of collisions becomes lower for the excitation collisions along the tangential trajectories of the H-ENAs).

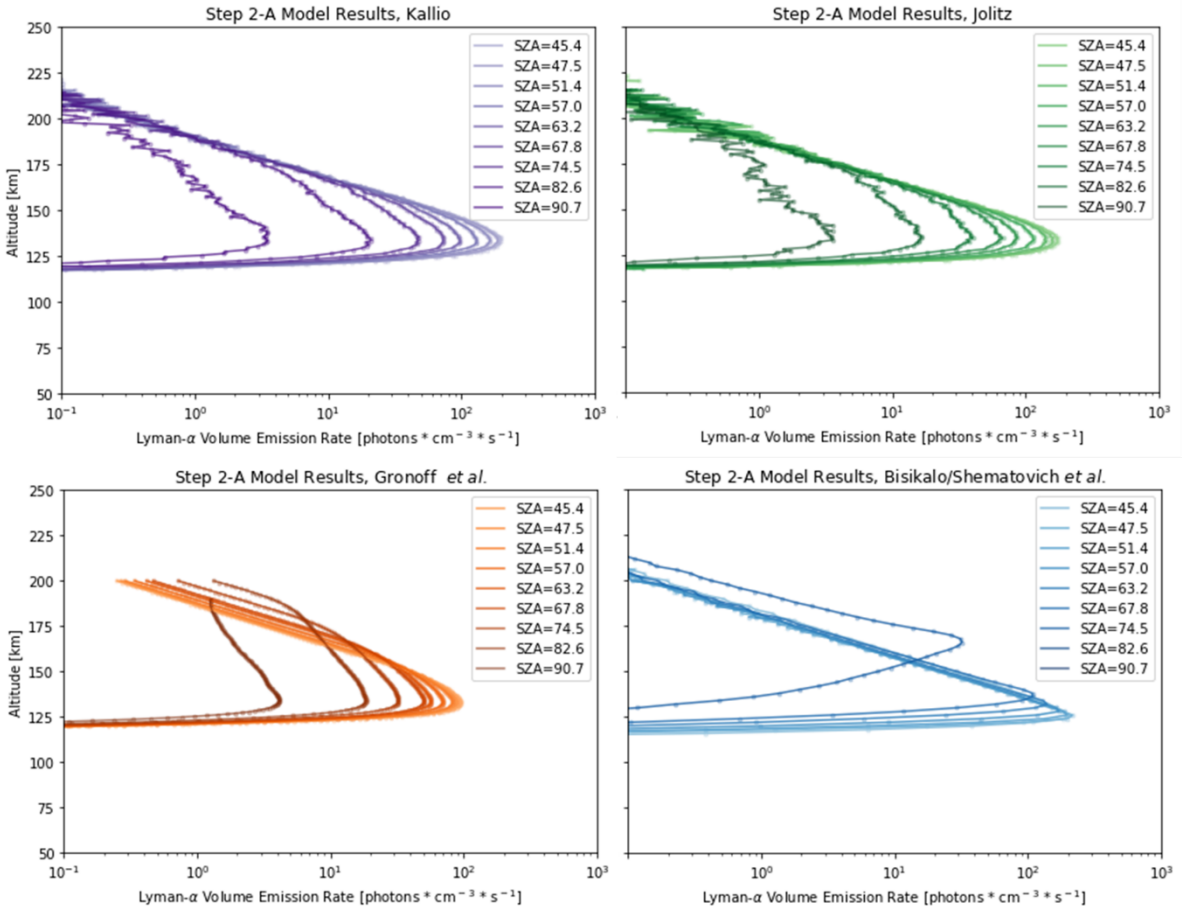

Figure 5: Simulation results from the data-model comparison step of the campaign (Step 2-A), showing proton aurora altitude-volume emission rate (VER) profiles from each model for the specified input parameters and SZAs. Most model results display similar peak altitudes and VERs agree with each other to within less than an order of magnitude. Note that SZA is decreasing from left-to-right between profiles in each panel.

4.6. Results of Step 2-B

Forward-modeling the simulation results using the radiative transfer model in Step 2-B allows a more direct comparison between the model results and the IUVS data. In so doing, we find through Step 2-B that the models effectively reproduce the general shape of the data, with some models overestimating and some underestimating the proton aurora brightness (Figure 6). All of the peak altitudes from the model results are ~5-15 km lower than the observed peak altitudes. The simulated intensities of the Gronoff *et al.* and Bisikalo/Shematovich *et al.* model results for

the low SZA profiles (*i.e.*, profiles on the right-most side of each plot) are ~1-1.5 kR higher and lower (respectively) than the proton aurora intensities observed in the data for similar SZA profiles. However, at high SZAs, all three models for which profiles exist appear to simulate the data intensities effectively. The Kallio and Jolitz model intensities overestimate the data by a few kR at low SZAs, while the Gronoff *et al.* model intensities underestimate by a few kR. At low SZAs, the Bisikalo/Shematovich *et al.* model intensities closely correlate with the data intensities, but still slightly overestimate the data; however, the Bisikalo/Shematovich *et al.* intensities underestimate the data at high SZAs. While all models effectively simulate the shape and SZA variability of the data profiles, none of the model intensities match the data exactly (possible reasons for this discrepancy are discussed in the following section).

Significant peak altitude discrepancies between the models and the data are present in every model. This altitude discrepancy suggests that other processes/assumptions are not fully accounted for or understood in our evaluation of the results. In the following section, we examine numerous possible parameters that may contribute to the observed discrepancies between the data and the models.

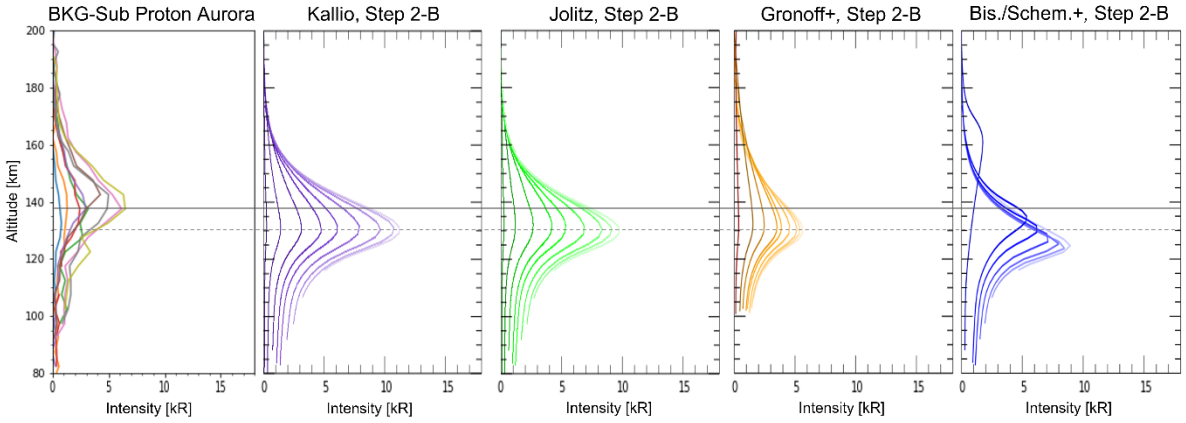

Figure 6: Simulation results for the data-model comparison after running the results through the radiative transfer model (Step 2-B). The background-subtracted (i.e., after subtracting out the theoretical "background" coronal H contribution) altitude-intensity profiles for this orbit are shown on the far left plot for comparison. The simulated proton aurora Ly-α intensities from each of the model results closely correlate with the data. However, note that there is still a discrepancy between the average peak altitude of the data profiles (solid grey horizontal line) and the average peak altitude of the model profiles (dashed grey horizontal line). Note also that the SZA of the observations is decreasing from left to right in all plots from SZA ~90° to SZA ~45° (i.e., moving toward the subsolar point), as shown in Figure 3 and Figure 5 legend.

5. Discussion of parameters affecting model differences and data-model discrepancies

5.1. Cross Section Processes and Scattering Angle Distributions

Differences in cross section and DSCS values are a probable partial contributor to the differences in the results simulated by each model. While the models in this study utilize the same five processes, most models do not use the same cross sections (see Figure 7 and Supplementary Table S1 for details). As shown in Figure 7, these values can change significantly with varying energy ranges. The cross section values used in each model agree to within less than an order of magnitude of each other for the relevant energy range in this study (*i.e.*, 100 eV – 2 keV). The most variable cross section across the models were those used for elastic collisions, with elastic cross sections used by the Bisikalo/Shematovich *et al.* and Gronoff *et al.* models exceeding those used by the Kallio and Jolitz models by a factor of ~5-8. These

differences can cause notable inter-model variability. Since many processes have not been measured in a laboratory for proton/H collisions with CO_2, an interpolated or substitute value is used for protons/H with O_2 or N_2. Particularly few measurements of protons with CO_2 are available for Ly-α. Comparable cross section values are a likely cause for the similarities observed between the Jolitz and Kallio results, and also a likely cause for the minor variability between these two models in the data-model comparison (*i.e.*, the Jolitz model uses smaller Ly-α cross sections at low energies and exhibits intensities that are 1-2 kR smaller than those of the Kallio model at low SZAs).

Different implementations of scattering can also cause inter-model variations. A model that assumes that a particle travels in the same direction before and after a collision ("forward scattering") will predict deeper particle penetration than a model that predicts variability in scattering angle. Introducing even a small probability of non-forward scattering reduces the precipitating flux and resulting emission rate. This is done by converting measured DSCS into a phase function evaluated during a model run. In this study, each model uses different ways to predict scattering (see supplementary material Text S1-S4 for detailed model descriptions). Kallio and Jolitz use the same phase function to predict non-zero scattering angles after elastic collisions, while all other collisions are assumed to be forward scattering. This, in tandem with the same model approach (3-D Monte Carlo) likely contributes to their similar model predictions. In contrast, the two 1-D kinetic Boltzmann solver models have slightly different scattering models. Gronoff *et al.* uses a screened Rutherford phase function with a fixed screening parameter in charge transfer and elastic collisions and assumes forward scattering in ionization collisions. Bisikalo/Shematovich *et al*. uses the same assumptions for all collisions except charge transfer, for which the model uses energy-dependent DSCS. The inclusion of non-forward scattering in these 1-D models could be responsible for the lower intensities predicted by these models compared to those predicted by the 3-D Monte Carlo models.

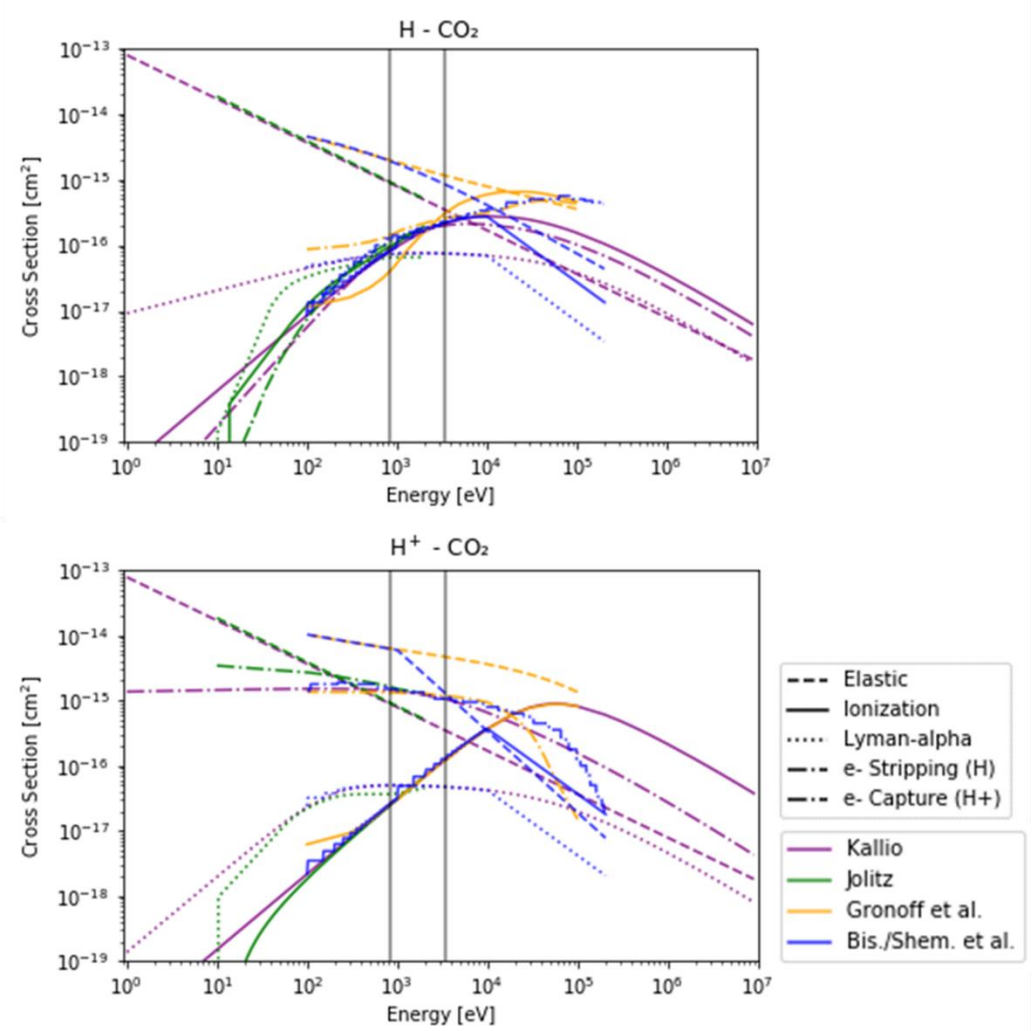

Figure 7: Available cross section values used by each modeling team (denoted by color) for the five different overlapping cross section processes considered in this study (denoted by line style). The solid vertical lines (grey) indicate the energy ranges evaluated in the representative cases in Step 1 assuming average (400 km/s) and high (800 km/s) solar wind velocities. See Supplementary Table S1 for more information regarding the cross section processes and relevant references in each model.

5.2. Data Quality and Caveats

In addition to the possible sources of discrepancy in the model assumptions, we must also consider possible caveats associated with the datasets. Because IUVS is a remote sensing instrument, its limb scan observations are created by integrating along the line of sight of the instrument. However, the SWIA penetrating proton fluxes are measured *in situ* during periapsis, and the orbit averaged value is used in this study. Because of the uniform nature of the processes creating proton aurora across the dayside of the planet it is appropriate to combine these datasets; nevertheless, there may be spatial and/or temporal discrepancies between these observations, even though the data were acquired during the same MAVEN orbit.

Secondly, because IUVS Level 1C (L1C) data are processed and altitude-binned, we note that minor discrepancies may be introduced in the Ly-α intensities during the data reduction process. Calibrated IUVS L1C data are reported with a systematic uncertainty between ~10-20%. As the results of this study are sensitive to the absolute calibration of the instrument, we must

also consider any possible uncertainties in the IUVS reported intensities as a potential source of discrepancy in the model-data comparison.

5.3. Other Assumptions

There are a number of additional assumptions in this study that may have led to discrepancies between the models and the data. First, numerous data-driven assumptions are made in creating the theoretical CO_2 density profile for Step 2. Any of three variables could be altered that could in turn significantly affect the proton aurora profile: the energy of the incident particles, the density of the atmosphere at the reference altitude, or the neutral atmospheric scale height. All of these variables affect the peak altitude of the proton aurora profile, while changing the scale height and energy also affects the profile peak intensity (more specifically, changing the scale height can also affect how broad/narrow the profile shape becomes). Observations made by MAVEN/SWIA during this orbit provide confidence that the calculation of particle energy (based on average penetrating proton velocity) and the assumption of monoenergetic particle behavior are appropriate/accurate, and therefore do not significantly affect the results. However, in this study we determine the atmospheric density at the reference altitude (130 km) by extrapolating from the average derived IUVS Level 2 CO_2 density at 130 km. Because the spherically symmetric CO_2 density profile used by modelers in this study is theoretically derived, inaccuracies in the assumed quantities for reference density or scale height would lead to an inaccurate representation of the atmospheric density profile during this time. Thus, it is possible that the CO_2 density profile is not entirely accurate in representing the atmosphere at this time, possibly contributing to some of the discrepancies observed in the data-model comparison. Moreover, only one neutral species (CO_2) is considered in our models, whereas other minor species (*e.g.*, CO, O_2 and O) should also contribute to some extent to the observed profiles (in a potentially important way, depending on altitude and latitude/longitude). Since H^+/H cross sections can vary significantly depending on the target neutral species (both in peak energy and intensity), the modeling results presented may be modified further if these species are included. We note, however, that because CO_2 is the overwhelmingly dominant species in the Martian atmosphere, the inclusion of minor species should not alter any of the primary findings presented in this study (but may decrease the observed discrepancies between the data and models). Such an added complexity is outside the scope of the present study and a more in-depth investigation of the inter-model's sensitivity to the neutral atmosphere composition is left for the future.

For simplicity in Step 2 we assume that the precipitating particle population at the top of each model atmosphere is entirely composed of H-ENAs. Although the incident particle population is indeed comprised of a fractionated portion of both ENAs and protons, this simplified assumption is preferred over a non-empirical assumption of an estimated fractionation ratio. Moreover, as the results in Step 1 do not significantly change in most models based on the assumption of an entirely H-ENA- or proton-rich population, we would not expect the effects of this assumption on its own to have a significant impact on the final results. One potential exception may be for the Bisikalo/Shematovich *et al.* results in which the peak intensity somewhat increases if a particle population of entirely protons is assumed (as seen in Step 1-A and 1-B). Because the Bisikalo/Shematovich *et al.* results showed slight variability based on the assumed incident particle population, it is possible that the intensities in their model results might be larger if this assumption is changed (which may cause their simulated intensities to more closely resemble those of the Kallio and Jolitz models, but to further overestimate the data intensities in Step 2).

The chosen method for calculating the ENA flux may be a contributor to the observed discrepancies between the data and model intensities. The H-ENA flux used in Step 2 is calculated as an empirically derived multiple of the orbit-averaged SWIA penetrating proton flux. While this ratio is supported by previous SWIA observations (*e.g.*, Halekas *et al.*, 2015; Halekas, 2017), the value can vary based on seasonal or other changes (*e.g.*, the solar wind proton flux, the neutral atmospheric scale height, or the location of the bow shock). As determined in Step 1, decreasing the flux by an order of magnitude (which is the typical variability observed throughout a Martian year, *e.g.*, Halekas, 2017) will correspondingly decrease the proton aurora peak intensity by an order of magnitude. Thus, although the method used to calculate the ENA flux is believed to be an accurate and statistically robust approximation, any major deviation from the statistical norm of local conditions during this orbit would cause discrepancies in accurately calculating the H-ENA flux.

Another possible contributor to the data-model discrepancies is the assumption of the monodirectional movement of the incident particles in the atmosphere. We include a terminology note here that in specifying "monodirectional" particle movement, we refer to the bulk velocity (*i.e.*, average speed and direction) of the precipitating particles. All modeling teams represented the incident precipitating particles as having a velocity fixed in magnitude (*e.g.*, 400 km/s and 800 km/s) and direction (anti-sunward). However, in reality the incident solar wind has nonzero temperature, and has a broader variability than modeled. While some model teams investigated the potential effects of this variability on the proton aurora profile (*e.g.*, Supplementary Figure S4), the results are preliminary and will be reviewed in further detail in a future study.

In this study we do not consider the effects of electric or magnetic fields (*i.e.*, IMF, induced, and/or crustal magnetic fields) on proton aurora. While most of the models do not predict any likely significant change on the proton aurora profile caused by magnetic fields, a previous modeling study by Gérard *et al*. (2019) (which utilized the Bisikalo/Shematovich *et al*. proton/hydrogen precipitation model) predicted a decrease in the peak brightness of the proton aurora profile in the presence of an induced magnetic field (*e.g.*, tens of nT). Comparatively, a recent study by Henderson *et al*. (2022) that evaluated the effects of magnetic fields on MAVEN/SWIA observations of penetrating protons suggests that only the very strongest magnetic fields (*e.g.*, strengths greater than 200 nT) are expected to have a notable influence on penetrating proton fluxes (*i.e.*, they did not find a significant influence for magnetic field strengths on the order of 10 nT). Since the IMF magnitude during the MAVEN orbit included in this study is non-negligible (*i.e.*, ~10 nT), it is possible that excluding magnetic/electric fields from our study may contribute to some of the observed model-data discrepancies. However, further analysis is required in order to understand the effects of magnetic fields (and variability in field strengths) on the proton aurora profile.

Lastly, we also do not consider the effects of particle backscattering on the results of this study. Because recent SWIA studies have shown that a significant portion of the incident particle population can be backscattered (Girazian and Halekas, 2021), this factor could thereby contribute to the data-model discrepancies (*e.g.*, potentially causing a lower observed proton aurora brightness in the data than what is predicted by models). However, determining the relative abundances of the forward- and back-scattered particle populations is outside the purview of this study and thus the potential impacts on model results are not quantified herein.

5.4. Unique model Capabilities and Insights

As previously stated, the purpose of this campaign is not to identify the best or most accurate model in the study, but rather, to characterize the ways in which each of the models uniquely excel. In this section we identify aspects of each model that make them distinctively capable in simulating proton aurora observations, as well as reasons for strong agreement/disagreement between the models.

A few important aspects to consider are the cross sections used in each model, the differences in the way the 3-D and 1-D solvers work, and how the relevant physics is treated. The Monte Carlo solving techniques (*e.g.*, collision by collision determinators) and cross sections used in the Kallio and Jolitz models are very similar (*e.g.,* Figure 7 and Supplementary Table S1), leading to the observed similarities in their model results. In contrast to these two models, the Bisikalo/Shematovich *et al.* and Gronoff *et al*. models generate outputs by solving coupled proton-hydrogen kinetic Boltzmann transport equations. The Bisikalo/Shematovich *et al.* model, which also uses Monte Carlo solving techniques, likely exhibits different results than the former two models because of the use of different cross sections and 1-D model dimensionality. The Gronoff *et al*. kinetic transport model uses cross section values different than those of other models and a unique 1-D multistream kinetic transport solver. Nevertheless, considering the variety of assumptions and technical implementations included in each model, it is striking how well all of the models agree with each other as well as with the data.

The Bisikalo/Shematovich *et al.* model is the only one to simulate results that display variability with SZA in the profile peak altitude: at low SZAs their simulated peak altitudes are the furthest from the data peak altitudes, but at some higher SZAs their simulated peak altitudes are closest to those of the data out of all models. Their model is unique in its incorporation of the physics associated with this variability. However, we note that the peak altitudes simulated by their model at very high SZAs are considerably higher than those typically observed for proton aurora (*e.g.*, Hughes *et al*., 2019).

The differences between the model results in the data-model comparison step demonstrate the capabilities, assumptions, and methodologies of each of the models. The Gronoff *et al*. and Bisikalo/Shematovich *et al.* models seem to be especially apt at approximating the data intensities at lower SZAs (although the Bisikalo/Shematovich *et al.* simulated intensities diverge the most at high SZAs). All models predict results which appropriately represent the decrease in Ly-α brightness with increasing SZA: the Kallio, Jolitz, and Gronoff *et al*. models appear to most accurately simulate this intensity falloff. The Bisikalo/Shematovich *et al.* model appears to be particularly efficient at simulating the relative intensity differences between profiles at lower SZAs, but the Jolitz model appears to be most consistently efficient across all SZAs. While all models are effective at simulating the data, none of the four particle precipitation models - which results are then run through the radiative transport model - can exactly reproduce the analyzed Ly-α peak intensities and altitudes measured by the IUVS instrument during MAVEN orbit 4235. This may indicate that the input parameters may not accurately represent the situation in the presented case, that the cross sections used may contain noticeable inaccuracies, and/or that some physical processes which are not included into the models play an important role in proton aurora formation.

6. **Conclusions and Future Work**

The results of this modeling campaign provide a new understanding of the primary factors influencing variability in Martian proton aurora. We identify the relative importance of

different input parameters on the proton aurora profile, finding the solar wind particle flux and velocity to be the most influential parameters affecting the profile shape, brightness, and peak altitude. Through undertaking this comparative study, we better constrain the driving processes of proton aurora as characterized by each contributing model; additionally, we determine the influence of model capabilities, solving techniques, and input assumptions on effectively reproducing proton aurora observations, and the dominant physics that needs to be incorporated in future modeling studies in order to accurately represent these events. Moreover, the results of this study are applicable more broadly than proton aurora at Mars, as similar auroral processes could occur on any planetary body that exhibits an extensive neutral H corona. Modeling studies such as this one are particularly important in efforts to study planetary bodies with minimal observations or where data are not available, both within our solar system and beyond (*e.g.*, Venus, comets, and exoplanets).

In a future study, we aim to address the effects of magnetic and electric fields on proton aurora. It will also be important to quantify the effect of the backscattered penetrating particle population on the proton aurora profile; since the models in this study can readily take into account collisional angular redistributions, incorporating these effects into the models would be feasible and relevant. Evaluating the effects of the monodirectional particle movement assumption (*e.g.*, by varying the incident particle bulk velocity/temperature) should also be considered in a future study. We note that this study depends strongly on consideration of the efficiency of charge exchange between protons in the undisturbed solar wind and H in the extended corona (as this is an upper boundary for calculations due to the precipitation of H-ENAs). Therefore, another possible next step for this campaign could be to consider the variations present in an energy spectrum of incident H atoms and protons (*i.e.*, an energy spectrum that is not monoenergetic). Additionally, major changes in the neutral atmospheric scale height (*e.g.*, local or global dust storms) can affect absorption by CO_2 on the bottom side of the proton aurora profile. Because absorption of Ly-α by CO_2 becomes significant below the peak of the proton aurora Ly-α emitting layer, it can have a non-trivial effect on proton aurora modeling efforts, potentially causing apparently lower peak intensities and higher peak altitudes in proton aurora profiles. We plan to address these effects of CO_2 absorption on the proton aurora profile in more detail. A future study could also potentially include creating a more detailed neutral model atmosphere to use in the models (*e.g.*, including SZA variability), or perhaps looking at nadir observations of proton aurora, which may help to bridge the gap between *in-situ* and remote sensing observations. Finally, it would be interesting to expand our analysis to include an "atypical" example of a proton aurora event in the data-modeling portion of the campaign (*e.g.*, spatially and/or temporally varying, nightside detections, etc.).

The MAVEN mission continues to make new and exciting observations of Martian proton aurora, and new Mars missions with UV instrument capabilities are also beginning to make contemporaneous observations of these events. As the current solar cycle increases toward solar maximum (a period corresponding with larger and more frequent solar activity), we anticipate that the intensity and frequency of proton aurora events at Mars will also increase correspondingly (*e.g.*, Hughes *et al.*, 2019). Thus, it is imperative in our efforts to study proton aurora that we first develop a firm knowledge of the physics and driving processes through modeling these events; this understanding will provide important context for future efforts to effectively model new and unique auroral observations at Mars.

Acknowledgments and Data Availability

The MAVEN mission is supported by NASA through the Mars Exploration Program in association with the University of Colorado and NASA's Goddard Space Flight Center. The work of GG and BH was supported by the NASA grant 80NSSC20K1348. CSW is funded by Austrian Science Fund (FWF) project P35954-N. EK acknowledges support from the Academy of Finland (Decisions No. 348784 and No. 310444). VS and DB acknowledge the financial support of the Russian Science Foundation, grant # 22-12-00364. JCG acknowledges support from the PRODEX program of ESA managed with the help of the Belgian Federal Scientific Policy Office (BELSPO).

In this study we use MAVEN/IUVS Level 1C version 13 altitude-binned periapsis data. This work utilized the RMACC Summit supercomputer, which is supported by the National Science Foundation (awards ACI-1532235 and ACI-1532236), the University of Colorado Boulder, and Colorado State University. The Summit supercomputer is a joint effort of the University of Colorado Boulder and Colorado State University.

All daytime Level 1C IUVS data products are publicly available from the Planetary Atmospheres node of the Planetary Data System (PDS) (https://pds-atmospheres.nmsu.edu/data_and_services/atmospheres_data/MAVEN/maven_iuvs.html). Similarly, MAVEN/SWIA (https://pds-atmospheres.nmsu.edu/data_and_services/atmospheres_data/MAVEN/swia.html) and MAVEN/NGIMS (https://pds-atmospheres.nmsu.edu/data_and_services/atmospheres_data/MAVEN/ngims.html) data are also available from the PDS. All MAVEN instrument Software Interface Specification (SIS) documents can be found on the before-mentioned PDS websites. The ATMOCIAD (Atomic and Molecular Cross section for Ionization and Aurora Database) database used in the Aeroplanets model (Gronoff *et al.*, 2021) is available at https://doi.org/10.5281/zenodo.4632426.

We would like to thank our collaborators on the MAVEN and IUVS Teams, especially Meredith Elrod and Robin Ramstad, for their contributions in understanding the local Mars environment during the time period of interest.

References

Anderson, D. E., and Hord, C. W. (1971). Mariner 6 and 7 Ultraviolet Spectrometer Experiment: Analysis of hydrogen Lyman-alpha data, *J. Geophys. Res.*, 76 (28), 6666– 6673, doi:10.1029/JA076i028p06666.

Bertaux, J.-L., Leblanc, F., Witasse, O., Quemerais, E., Lilensten, J., Stern, S. A., … Korablev, O. (2005), Discovery of an aurora on Mar, *Nature*, 435(7043), 790–794, doi: 10.1038/nature03603.

Bisikalo D.V., Shematovich V.I., Gérard J.-C., Hubert B. (2018), Monte Carlo simulations of the interaction of fast proton and hydrogen atoms with the Martian atmosphere and comparison with in situ measurements, *Journal of Geophysical Research: Space Physics*, V. 123, Issue 7, pp. 5850-5861.

928 Chaffin, M. S., J.-Y. Chaufray, I. Stewart, F. Montmessin, N. M. Schneider, and J.-L. Bertaux
929 (2014), Unexpected variability of Martian hydrogen escape, *Geophysical Research*
930 *Letters*, *41*(2), 314-320, doi:10.1002/2013gl058578.

931 Chaffin, M.S., Kass, D.M., Aoki, S. et al. Martian water loss to space enhanced by regional dust
932 storms. Nat Astron 5, 1036–1042 (2021). https://doi.org/10.1038/s41550-021-01425-w

933 Clarke, J. T., J. L. Bertaux, J. Y. Chaufray, G. R. Gladstone, E. Quémerais, J. Wilson, and D.
934 Bhattacharyya (2014), A rapid decrease of the hydrogen corona of Mars, *Geophysical*
935 *Research Letters*, *41*(22), 8013-8020.

936 Deighan, J, S. K. Jain, M. S. Chaffin, X. Fang, J. S. Halekas, J. T. Clarke, N. M. Schneider, A. I.
937 F. Stewart, J.-Y. Chaufray, J. S. Evans, M. H. Stevens, M. Mayyasi, A. Stiepen, M.
938 Crismani, W. E. McClintock, G. M. Holsclaw, D. Y. Lo, F. Montmessin, F. Lefevre, B.
939 M. Jakosky (2018), Discovery of Proton Aurora at Mars, *Nature Astronomy*, 2(10), 802.

940 England, S. L., Liu, G., Withers, P., Yiğit, E., Lo, D., Jain, S., ... and Elrod, M., (2016),
941 Simultaneous observations of atmospheric tides from combined in situ and remote
942 observations at Mars from the MAVEN spacecraft, *J. Geophys. Res.: Planets*, Volume
943 121, Issue 4, pp. 594-607.

944 Galand, M., J. Lilensten, W. Kofman, and R. B. Sidje (1997), Proton transport model in the
945 ionosphere 1. Multistream approach of the transport equations, *Journal of Geophysics*
946 *Research*, 102, 22261–72, https://doi.org/10.1029/97JA01903.

947 Galand, M., J. Lilensten, W. Kofman, and D. Lummerzheim (1998), Proton transport model in
948 the ionosphere. 2. Influence of magnetic mirroring and collisions on the angular
949 redistribution in a proton beam, *Annales Geophysicae*, 16, 1308–21,
950 https://doi.org/10.1007/s00585-998-1308-y.

951 Gérard J.-C., Hubert B., Bisikalo D.V., and Shematovich V.I. (2000), Lyman-alpha emission in
952 the proton aurora. *J. Geophys. Res.*, V. 105, No. A7, 15795.

953 Gérard, J. C., B. Hubert, B. Ritter, V. I. Shematovich, D. V. Bisikalo (2019), Lyman-α emission
954 in the Martian proton aurora: Line profile and role of horizontal induced magnetic field,
955 *Icarus*, 321, 266-271.

956 Girazian and Halekas (2021), Precipitating Solar Wind Hydrogen at Mars: Improved
957 Calculations of the Backscatter and Albedo with MAVEN Observations, *J. Geophys.*
958 *Res.: Planets*, Volume 126, Issue 2, doi: 10.1029/2020JE006666.

959 Gronoff, G., C. Simon Wedlund, C. J. Mertens, and R. J. Lillis (2012a), "Computing
960 uncertainties in ionosphere-airglow models: I. Electron flux and species production
961 uncertainties for Mars", *Journal of Geophysical Research: Space Physics*, 117 (April):
962 4306, 18 PP., https://doi.org/10.1029/2011JA016930.

963 Gronoff, G., C. Simon Wedlund, C. J. Mertens, M. Barthélemy, R. J. Lillis, and O. Witasse
964 (2012b), "Computing Uncertainties in Ionosphere-Airglow Models: II. The Martian
965 Airglow", *J. Geophys. Res.* 117 (May): 17 PP.
966 https://doi.org/201210.1029/2011JA017308.

967 Gronoff, G., B. Hegyi, C. Simon Wedlund, & J. Lilensten. (2021), "The ATMOCIAD database",
968 *Zenodo*. https://doi.org/10.5281/zenodo.4632426

969 Halekas, J. S., E. R. Taylor, G. Dalton, G. Johnson, D. W. Curtis, J. P. McFadden, D. L.
970 Mitchell, R. P. Lin, B. M. Jakosky (2013), The Solar Wind Ion Analyzer for MAVEN,
971 *Space Science Rev., 195*(1-4), 125-151.

972 Halekas, J. S., Lillis, R. J., Mitchell, D. L., Cravens, T. E., Mazelle, C., Connerney, J. E. P., ... &
973 Luhmann, J. G. (2015), MAVEN observations of solar wind hydrogen deposition in the
974 atmosphere of Mars, *Geophys. Res. Lett.*, 42, 8901–8909, doi: 10.1002/2015GL064693.

975 Halekas, J. S. (2017), Seasonal variability of the hydrogen exosphere of Mars, *J. Geophys. Res.:*
976 *Planets*, 122, 901–911, doi: 10.1002/2017JE005306.

977 Henderson, S., Halekas, J., Girazian, Z., Espley, J., & Elrod, M. (2022), Influence of magnetic
978 fields on precipitating solar wind hydrogen at Mars, Geophysical Research Letters, 49,
979 e2022GL099114. https://doi.org/10.1029/2022GL099114.

980 Huestis, D.L., and J. Berkowitz, (2010). Critical evaluation of the photoabsorption cross section
981 of CO2 from 0.125 to 201.6 nm at room temperature, *Advances in Geosciences* Vol. 25:
982 Planetary Science 229-242

983 Hughes, A., Chaffin, M., Mierkiewicz, E., Deighan, J., Jain, S., Schneider, N., (2019), Proton
984 aurora on Mars: A dayside phenomenon pervasive in southern summer, *J. Geophys. Res.:*
985 *Space Physics*, 124, 10,533–10,548, doi: 10.1029/2019JA027140.

986 Hunten, D.M., F.E. Roach, and J.W. Chamberlain, (1956). A photometric unit for the airglow
987 and aurora, *Journal of Atmospheric and Terrestrial Physics*, Volume 8, Issue 6, Pages
988 345-346, https://doi.org/10.1016/0021-9169(56)90111-8.

989 Jakosky, B. M., Lin, R. P., Grebowsky, J. M., Luhmann, J. G., Mitchell, D. F., Beutelschies, G.,
990 ... & Baker, D. (2015), The Mars atmosphere and volatile evolution (MAVEN) mission,
991 *Space Sci. Rev.*, 195(1-4), 3-48.

992 Jolitz, R. D., C. F. Dong, C. O. Lee, R. J. Lillis, D. A. Brain, S. M. Curry, S. Bougher, C. D.
993 Parkinson, and B. M. Jakosky (2017), A Monte Carlo model of crustal field influences on
994 solar energetic particle precipitation into the Martian atmosphere, J. Geophys. Res. Space
995 Physics, 122, 5653–5669, doi:10.1002/2016JA023781.

996 Jolitz, R. D., Dong, C. F., Rahmati, A., Brain, D. A., Lee, C. O., Lillis, R. J., Curry, and B. M.
997 Jakosky (2021), Test particle model predictions of SEP electron transport and
998 precipitation at Mars, *Journal of Geophysical Research: Space Physics*, 126,
999 e2021JA029132, https://doi. org/10.1029/2021JA029132

1000 Kallio, E., and S. Barabash (2000), On the elastic and inelastic collisions between precipitating
1001 energetic hydrogen atoms and Martian atmospheric neutrals J. Geophys. Res., 105,
1002 24,973-24,996.

1003 Kallio, E., & Barabash, S. (2001), Atmospheric effects of precipitating energetic hydrogen atoms
1004 on the Martian atmosphere, *J. Geophys. Res.: Space Physics*, *106*(A1), 165-177, doi:
1005 10.1029/2000JA002003.

1006 Lo, D. Y., Yelle, R. V., Schneider, N. M., Jain, S. K., Stewart, A. I. F., England, S. L., ... &
1007 Chaffin, M. S. (2015), Nonmigrating tides in the Martian atmosphere as observed by
1008 MAVEN IUVS, *Geophys. Res. Lett.*, 42(21), 9057-9063.

1009 Mahaffy, P.R., Benna, M., King, T. *et al.* The Neutral Gas and Ion Mass Spectrometer on the
1010 Mars Atmosphere and Volatile Evolution Mission. *Space Sci Rev* **195,** 49–73 (2015).
1011 https://doi.org/10.1007/s11214-014-0091-1

1012 McClintock, W. E., N. M. Schneider, G. M. Holsclaw, J. T. Clarke, A. C. Hoskins, I. Stewart, F.
1013 Montmessin, R. V. Yelle (2015), The Imaging Ultraviolet Spectrograph (IUVS) for the
1014 MAVEN Mission, *Space Sci. Rev.*, doi: 10.1007/s11214-014-0098-7.

1015 Ritter, B., J.-C. Gérard, B. Hubert, L. Rodriguez, and F. Montmessin (2018), Observations of the
1016 proton aurora on Mars with SPICAM on board Mars Express, *Geophys. Res. Lett.*, 45.
1017 doi: 10.1002/2017GL076235.

1018 Schneider, N. M., J. I. Deighan, S. K. Jain, A. Stiepen, A. I. F. Stewart, D. Larson, D. L.
1019 Mitchell, C. Mazelle, C. O. Lee, and R. J. Lillis (2015), Discovery of diffuse aurora on
1020 Mars, *Science, 350*(6261), aad0313.

1021 Shematovich V. I., D. V. Bisikalo, C. Diéval, S. Barabash, G. Stenberg, H. Nilsson, Y. Futaana,
1022 M. Holmstrom, and J.-C. Gérard. (2011), Proton and hydrogen atom transport in the
1023 Martian upper atmosphere with an induced magnetic field, *J. Geophys. Res.*, V. 116,
1024 Issue A11, CiteID A11320.

1025 Shematovich V.I., Bisikalo D.V., Gérard J.-C., Hubert B. (2019), Kinetic Monte Carlo model of
1026 the precipitation of high-energy proton and hydrogen atoms into the Martian atmosphere
1027 with taking into account the measured magnetic field, *Astronomy Reports*, Vol. 63, No.
1028 10, pp. 835–845.

1029 Simon, Cyril. (2006), "Contribution à L'étude Des Entrées d'énergie Solaire Dans L'ionosphère:
1030 Ions Doublement Chargés et Transport Cinétique Des Protons - Application à La Terre et
1031 à Titan." PhD thesis, Université Joseph-Fourier - Grenoble I. http://tel.archives-
1032 ouvertes.fr/tel-00109802.

1033 Simon, C., J. Lilensten, J. Moen, J. M. Holmes, Y. Ogawa, K. Oksavik, and W. F. Denig (2007),
1034 "TRANS4: a new coupled electron/proton transport code - comparison to observations
1035 above Svalbard using ESR, DMSP and optical measurements." Annales Geophysicae 25
1036 (March): 661–73. https://doi.org/10.5194/angeo-25-661-2007.

1037 Simon Wedlund, C., G. Gronoff, J. Lilensten, H. Ménager, and M. Barthélemy (2011),
1038 "Comprehensive calculation of the energy per ion pair or W values for five major
1039 planetary upper atmospheres." Annales Geophysicae 29 (January): 187–95.
1040 https://doi.org/10.5194/angeo-29-187-2011.

1041 Stone, S. W., Yelle, R. V., Benna, M.,Elrod, M. K., & Mahaffy, P. R. (2018),Thermal structure
1042 of the Martianupper atmosphere from MAVENNGIMS.Journal of GeophysicalResearch:
1043 Planets,123, 2842–2867.https://doi.org/10.1029/2018JE005559.

JGR: Space Physics

Supporting Information for

Advancing our Understanding of Martian Proton Aurora through a Coordinated Multi-Model Comparison Campaign

Andréa C. G. Hughes[1,2,3], Michael Chaffin[4], Edwin Mierkiewicz[3], Justin Deighan[4], Rebecca D. Jolitz[4], Esa Kallio[5], Guillaume Gronoff[6,7], Valery Shematovich[8], Dmitry Bisikalo[8,9], Jasper Halekas[10], Cyril Simon Wedlund[11], Nicholas Schneider[4], Birgit Ritter[12,13], Zachary Girazian[10], Sonal Jain[4], Jean-Claude Gérard[12], and Bradley Hegyi[6,7]

[1] NASA Goddard Space Flight Center, Greenbelt, MD, United States.
[2] Department of Physics & Astronomy, Howard University, Washington, DC, United States.
[3] Center for Space and Atmospheric Research (CSAR) and the Department of Physical Sciences, Embry-Riddle Aeronautical University, Daytona Beach, Florida, United States.
[4] Laboratory for Atmospheric and Space Physics, University of Colorado, Boulder, CO, USA. United States.
[5] Aalto University, School of Electrical Engineering, Department of Electronics and Nanoengineering, Espoo, Finland.
[6] NASA Langley Research Center, Hampton, VA, United States.
[7] Science Systems and Application Inc. Hampton, VA, United States.
[8] Institute of Astronomy of the Russian Academy of Sciences, Moscow, Russia.
[9] National Center for Physics and Mathematics, Russian Federation, Moscow, Russia.
[10] Department of Physics and Astronomy, University of Iowa, Iowa City, IA, United States.
[11] Space Research Institute, Austrian Academy of Sciences, Graz, Austria.
[12] Royal Observatory of Belgium, Brussels, Belgium.
[13] Université de Liège, LPAP – STAR Institute, Liege, Belgium.

Contents of this file

Introduction

Herein we provide supplemental materials regarding the models used in the study, cross sections used in the models, and additional information regarding the locations of MAVEN and MAVEN/IUVS for observations taken during the orbit of interest. In the Supplementary Text section, we present detailed descriptions of each of the four proton/hydrogen precipitation models used in the study. Descriptions are written by each modeling team and appropriate references are given at the end of each section. In the Supplementary Figures section, we present S1) maps showing the locations of the MAVEN spacecraft during the orbit used in this study (including comparative locations of strong crustal fields), S2) ephemeris data for the MAVEN/IUVS instrument while acquiring the periapsis limb scan data used in this study, S3) relevant profiles used for the coronal thermal H background subtraction method described in the text, and S4) preliminary results comparing the assumption of monodirectional incident particle movement versus isotropic. Lastly, we include a Supplementary Table with details regarding cross sections used by each model and relevant references.

Text S1.

Kallio 3-D Monte Carlo Model Description

(i) General introduction: nature of the model, brief history of its development, and general references

The Kallio model is described in detail in *Kallio and Barabash*, 2000 and 2001. The model is a 3-D Monte Carlo (MC) model where the incident particle, either H^+ or H, collides with neutral particles after which the velocity of the particle is changed. The model contains 6 elastic and 24 inelastic processes but, in this study, only the processes mentioned in the main text of this paper were used.

The model uses a Cartesian coordinate system both for the positions and velocities of the precipitating particles. In the coordinate system the x-axis points from the center of Mars toward the Sun.

(ii) Inputs, processes included (with relevant cross section references), and outputs

The model inputs are neutral atom densities, energy dependent total cross-sections (CS), the differential scattering cross-sections (DSCS), the number of precipitating particles (N_H), and the initial positions ($\boldsymbol{r}_{particle}(t=0)$) and velocities ($\boldsymbol{v}_{particle}(t=0)$) of the precipitating particles -- in the present case hydrogen atoms (H).

The total cross sections are given in *Kallio and Barabash, 2001* (Table 1 and Fig. 3) and the DSCS scattering angle distribution in *Kallio and Barabash*, 2000 (Fig. 1, "nominal") and 2001 (Fig. 2). Total cross sections give the probability that a collision

occurs. Random numbers are used to model if a collision occurs, and which collision process occurs. If a collision happens, then the DSCS determines the new velocity of the incident particle after collision. The value of the scattering angle is obtained by using a new random variable.

(iii) Implementation and technical aspects: assumptions and constraints, domain of applicability and grid description, spatial resolution and timesteps, number of particles, overall performance, etc.

In the simulation, particles are injected into the upper atmosphere at the point [x, y, z] = [260 km + R_{Mars}, 0, 0], where the radius of the Mars, R_{Mars}, was in the simulation 3393 km. The velocity of the particles in the analysis presented in this paper was a constant $\boldsymbol{v} = [v_x, v_y, v_z] = [-400, 0, 0]$ km/s, i.e., a beam of particles initially moving exactly along the Sun-Mars line.

The model saves the position and the velocity of the particle if it has a Ly-α collision process. The Ly-α volume production rate was derived from the saved positions of Ly-α processes by collecting the number of the Ly-α collision processes ($d\#_k^{hf}$) at a given altitude (h) range: $dh_k \equiv h_{k+1} - dh_k$. Then in Step 1 runs the Ly-α volume of the emission was derived by using a 1-D approximation, i.e., assuming that the area of the emission perpendicular to the x-axis (dA_{hf}) is equal to the initial area in the solar wind (dA_{sw}) through which the precipitating particles initially came, $dA_{hf} = dA_{sw}$. Note that the inaccuracy caused by the 1-D approximation, $dA_{hf} = dA_{sw}$, is small because the horizontal movement of the colliding particles in the atmosphere is small compared with the radius of the planet. Therefore, the volume (dV_k) from which the emission came within dh_k in Step 1 runs was assumed to be $dV_k = dh_k \times dA_{sw}$. In Step 2 runs the volume dV_k was derived without any approximations from the space angle and the altitude range.

The altitude dependent Ly-α volume emission rate

$$q_k^{hf} = d\#_k^{hf} / (dt \times dV_k) = d\#_k^{hf} / (dt \times dh_k \times dA_{hf}), \quad (1)$$

which, as mentioned above, was in Step 1 runs derived by approximating $dA_{hf} = dA_{sw}$

$$q_k^{hf} = d\#_k^{hf} / (dt \times dh_k \times dA_{sw}), \quad (2)$$

is finally obtained from the particle flux of the precipitating H particles (j_H), the number of the particles used in the MC simulation (N_H) and the time (dt) which takes N_H particles to go through the area dA_{sw}: $N_H = j_H\, dt \times dA_{sw}$. This gives $dt \times dA_{sw} = N_H / j_H$ and Eq (2) gets the form

$$q_k^{hf} = d\#_k^{hf} / (dt \times dV_k) = j_H\, [d\#_k^{hf} / (dh_k \times N_H)]. \quad (3)$$

In the analyzed simulation N_H was 5000 and 100,000 in Step 1 and Step 2 runs, respectively. As can be seen in Eq. (3) the particle flux j_H is just a scaling factor and in this paper, it was 10^7 cm^{-3} s^{-1}. In the plots presented in this paper the Ly-α emission altitude profiles were derived in 1 km altitude bins, i.e., $dh_k = 1$ km. This provided a relatively good compromise between modest statistical fluctuations and the accurate determination of the peak emission value and altitude.

(iv) Strengths and applications most suited for the model

The largest uncertainty for the obtained Ly-α volume emission rate q_k^{hf} is related to the uncertainty of the total cross-sections used and the differential scattering cross sections between H and H^+ particles and CO_2 molecules. In the simulation many of these

H/H^+ collisions with CO_2 are modeled with H/H^+ collisions with O_2 and N_2 which was published in the literature (see *Kallio and Barabash*, 2001, Table 1, for details).

As described in *Kallio and Barabash*, 2000 and 2001, functional forms of the adopted DSCS are modeled following *Noël and Prölss* (1993). The used DSCS (see *Kallio and Barabash*, 2000, Fig. 1a, the "nominal" DCSC and *Kallio and Barabash*, 2001, Fig. 2) is a fit to the data of $H - O_2$ collisions from *Newmann et al*., 1986, Table 4.

It is worth noting that although the statistical fluctuations in the derived emission altitude profiles could be reduced by using a larger number of precipitating particles in the 1 km altitude binning used, the statistical fluctuations are relatively modest already for the number of particles used.

It is also worth noting that the MC model used can be automatically used in future more complicated situations than done in this paper. In this study the precipitating particles formed a monoenergetic beam. However, the velocity distribution function can be more complicated; for example, a Maxwellian velocity distribution function, or the velocities can be read from a file. Moreover, the atmospheric density profile, $n(\boldsymbol{r})$ can be 2-D, say $n(\boldsymbol{r}) = n(\mathrm{SZA}, h)$. In such a case the MC model can be used to derive altitude profiles at a given SZA (see *Kallio and Barabash*, 2001, for details). The atmospheric density can also be 3-D, i.e., $n(\boldsymbol{r}) = n(x, y, z)$, which would result in the 3-D Ly-α emission rates. In the simulation the particle flux and their velocity distribution can also have latitude-longitude dependence (see *Kallio and Janhunen*, 2001, for details).

References:

Kallio, E., and S. Barabash, On the elastic and inelastic collisions between precipitating energetic hydrogen atoms and Martian atmospheric neutrals J. Geophys. Res., 105, 24,973-24,996, 2000.

Kallio, E., and S. Barabash, Atmospheric effects of precipitating energetic hydrogen atoms on the Martian atmosphere, J. Geophys. Res., 106, 165-178, 2001.

Kallio, E., and P. Janhunen, Atmospheric effects of proton precipitation in the Martian atmosphere and its connection to the Mars-solar wind interaction, J. Geophys. Res., 106, 5617-5634, 2001.

Newman, J. H., Y. S. Chen, K. A. Smith and R. F. Stebbings, Differential cross sections for scattering of 0.5-, 1.5-, and 5.0-keV hydrogen atoms by He, H2, N2, and O2, J. Geophys. Res., Volume 91, Issue A8, Pages 8947-8954,1986.

Noël, S. and G. W. Prölss, Heating and radiation production by neutralized ring current particles. J. Geophys. Res., Volume 98, Issue A10, Pages 17317-17325,1993.

Rees, M. H., Physics and Chemistry of the Upper Atmosphere, Cambridge Univ. Press, New York, 1989.

Rudd, M. E., Kim, Y. K., Madison, D. H., & Gallagher, J. W., Electron production in proton collisions: Total cross sections. Reviews of Modern Physics, 57, 965– 994, 1985.

Van Zyl, B., Neumann, H., Le, T. Q., and R.C. Amme, H + N2 and H + O2 collisions: Experimental charge-production cross sections and differential scattering calculations, Phys. Rev. A 18(2):506-516, 1978.

Van Zyl, B., and H. Neumann, Lyman α emission cross sections for low-energy H and H+ collisions with N2 and O2, J. Geophys. Res, 93(A2):1023-1027, 1988.

Text S2.

Jolitz 3-D Monte Carlo Model Description (Name: "ASPEN")

ASPEN (Atmospheric Scattering of Protons, Electrons, and Neutrals) is a 3-D Monte Carlo test particle simulation. This model was initially developed to predict atmospheric ionization rates at Mars by solar energetic particles, which have higher energies than the ENAs studied in this paper [Jolitz *et al.,* 2017] and has since been used to predict precipitating SEP electron fluxes at Mars [Jolitz *et al., 2021*]. The simulation solves the Lorentz force equations for energetic particle motion and uses a Monte Carlo approach to predict collisions and resulting energy loss in the atmosphere. Since magnetic fields were set to zero for this study, the transport equations reduced to ballistic motion.

The collisional energy degradation algorithm used in ASPEN was originally developed and described in Lillis *et al.* [2008] for an electron precipitation model. It is very similar to the Kallio model in approach. Stochastic collisions were modeled by inverting the relation between intensity, density, and absorption cross-section for a particle beam incident on a medium of scatterers (colloquially known as Beer's law) to dynamically calculate a probability distribution function that is combined with a random number to predict variable distances between collisions. This probability distribution function is calculated for each individual particle and depends on the position, path, and energy through the planetary atmosphere. Similarly, whenever a collision occurs, the type of collision is predicted probabilistically using the relative cross-section of each possible collisional process and the particle energy is decremented by the corresponding energy loss. As a particle loses energy, the relative cross-sections of each process change. For example, a 2 keV proton colliding with a carbon dioxide molecule has a roughly 70% likelihood of capturing an electron, but the likelihood for the same process when the proton is 20 eV is only 20%.

This model is highly dependent on the choice of cross-sections. For the application in this study, the selected cross-sections for hydrogen and proton impact on carbon dioxide are described in Jolitz *et al.* [2017], with one exception. The cross-sections for proton- and hydrogen-impact excitation was replaced with Lyman-alpha emission cross-sections. Unfortunately, experimental measurements of the Lyman-alpha emission cross-section from proton and hydrogen atom impact on carbon dioxide is limited. As of the time of this paper's writing, only one set of measurements exist for 1-25 keV protons and hydrogen atoms [Birely and McNeal, 1972]. The cross-section for emission by protons and hydrogen atoms below 1 keV is unknown. In order to approximate emission from particles at these energies, ASPEN uses a cross-section calculated by scaling the corresponding emission cross-sections from impact on molecular oxygen. ASPEN also accounts for the fact that proton-induced Lyman-alpha

emission can only occur in addition to a charge exchange collision, since Lyman-alpha can only be emitted by a hydrogen atom.

Since ASPEN is a 3-D Monte Carlo simulation, predicting an accurate emission rate requires appropriate choice of initial conditions and a large volume of simulated particles. For Step 1, we simulated 10,000 particles incident on the subsolar point from an altitude of 600 km and calculated the emission rate by binning all Lyman-alpha emitting collisions as a function of altitude and multiplying by the incident flux. For Step 2, we simulated 10,000 particles uniformly distributed in space on a plane perpendicular to the direction of solar wind flow. Each particle represents a fraction of the assumed incident flux. The emission rate was then calculated by weighing the total number of emissions binned by altitude, solar zenith angle, and the fraction of flux associated with each simulated particle.

References:

Avakyan, S. V., R. N. Il'in, V. M. Lavrov, and G. N. Ogurtsiv (1998), Collision Processes and Excitation of UV Emission From Planetary Atmospheric Gases: A Handbook of Cross Sections, Gordon and Breach, Amsterdam.

Barnett, C. F., Ray J. A., Ricci, E., Wilkers, M. I., et al. 1977. Atomic data for controlled fusion research. Report no. ORNL-5296. Oak Ridge, TN: Oak Ridge National Laboratory.

Birely, J.H., and R.J. McNeal (1972), Lyman-alpha emission cross sections for collisions of 1-25 keV H+ and H with CO, CO2, CH4, and NH3, J.Chem Phys., 56 (5), 2189-94, doi:10.1063/1.1677518.

Jolitz, R. D., C. F. Dong, C. O. Lee, R. J. Lillis, D. A. Brain, S. M. Curry, S. Bougher, C. D. Parkinson, and B. M. Jakosky (2017), A Monte Carlo model of crustal field influences on solar energetic particle precipitation into the Martian atmosphere, J. Geophys. Res. Space Physics, 122, 5653–5669, doi:10.1002/2016JA023781.

Jolitz, R. D., Dong, C. F., Rahmati, A., Brain, D. A., Lee, C. O., Lillis, R. J., Curry, and B. M. Jakosky (2021). Test particle model predictions of SEP electron transport and precipitation at Mars. *Journal of Geophysical Research: Space Physics*, 126, e2021JA029132. https://doi. org/10.1029/2021JA029132

Lillis, R. J., D. L. Mitchell, R. P. Lin, and M. H. Acuña (2008), Electron reflectometry in the Martian atmosphere, Icarus, 194(2) 544-61, doi:10.1016/j.icarus.2007.09.030.

McNeal, R.J. (1970), Production of positive ions and electrons in collisions of 1-25-keV protons and hydrogen atoms with CO, CO2, CH4, and NH3, J. Chem. Phys. 53, 4308.

Nakai, Y., T. Shirai, T. Tabata, and R. Ito (1987), Cross sections for charge transfer of hydrogen atoms and ions colliding with gaseous atoms and molecules, At. Data Nucl. Data Tables, 37, 69– 101, doi:10.1016/0092-640X(87)90005-2.

Newman, J. H., Chen, Y.S., Smith, K.A., and R.F. Stebbings (1986), Differential cross sections for scattering of 0.5-, 1.5-, and 5.0-keV hydrogen atoms by He, H2, N2, and O2, J. Geophys. Res. 91(A8), 8947–8954.

Noël S., and G. W. Prölss (1993), Heating and radiation production by neutralized ring current particles. J Geophys Res 98:17317–17325.

Rudd, M. E., Kim, Y. K., Madison, D. H., & Gallagher, J. W. (1985), Electron production in proton collisions: Total cross sections. Reviews of Modern Physics, 57, 965– 994.

Van Zyl, B., Neumann, H., Le, T. Q., and R.C. Amme (1978), H + N2 and H + O2 collisions: Experimental charge-production cross sections and differential scattering calculations, Phys. Rev. A 18(2):506-516.

Van Zyl, B., and H. Neumann (1988), Lyman α emission cross sections for low-energy H and H+ collisions with N2 and O2, J. Geophys. Res, 93(A2):1023-1027.

Text S3.

Bisikalo/Shematovich *et al.* 1-D Monte Carlo Model Description

The Bisikalo/Shematovich et al. model is a 1-D kinetic Monte Carlo model. The model considers three primary processes: 1) precipitation of high-energy hydrogen atoms and protons that lose their kinetic energy in the elastic and inelastic collisions, 2) ionization of target atmospheric molecules/atoms, and 3) charge transfer and electron capture collisions with the major atmospheric constituents (i.e., CO2, N2, and O). Secondary fast hydrogen atoms and protons carry enough kinetic energy to cycle through the collisional channels mentioned above and result in a growing set of translationally and internally excited atmospheric atoms and/or molecules.

To study the precipitation of high-energy H/H^+ flux into the planetary atmosphere, we solve the kinetic Boltzmann equations (Shematovich *et al.*, 2011) for H^+ and H, including the collision term:

$$\mathbf{v}\frac{\partial}{\partial \mathbf{r}} f_{H/H+} + \left(\mathbf{g} + \frac{e}{m_{H+}} \mathbf{v} \times \mathbf{B} \right) \frac{\partial}{\partial \mathbf{v}} f_{H/H+} = Q_{H/H+}(\mathbf{v}) + \sum_{M=O,N_2,CO_2} J_{mt}(f_{H/H+}, f_M). \quad (1)$$

Equation (1) is written in the standard form for the velocity distribution functions $f_{H/H+}(r,v)$, and $f_M(r,v)$ for hydrogen atoms and protons (Gérard *et al.*, 2000). The source term $Q_{H/H+}$ describes the production rate of secondary H/H^+ particles and the elastic and inelastic collisional terms J_{mt} for H/H^+ describe the energy and momentum transfer to the ambient atmospheric gas which is characterized by local Maxwellian velocity distribution functions. Our kinetic Monte Carlo model (Gérard *et al.*, 2000; Shematovich *et al.*, 2011) is used to solve kinetic equation (1). The model is 1-D in geometric space and 3-D in velocity space. Nevertheless, the 3-D trajectories of H/H^+ are calculated in the code with final projection on radial direction. In the current version of the MC model (Shematovich *et al.*, 2019) an arbitrary structure of the induced magnetic field of Mars is included; that is, all three components of the magnetic field **B** = *{Bx,By,Bz},* were taken into account. The details of the model implementation and statistics control with the variance below 10% can be found in (Shematovich *et al.*, 2019).

The essence of the kinetic Monte Carlo model is accounting of all possible collisions in the atmospheric region studied. Therefore, statistics for all collisional processes are accumulated during the numerical realization of the kinetic model of the proton aurora. It provides a good basis for the evaluation of the Ly-α source functions as keeping of all excitation processes and their spatial characteristics makes it possible to determine the statistical distribution of the emitted Ly-α photons.

The energy deposition rate of H/H+ flux is determined by the cross sections of the collisions with the ambient gas. The energy lost by the H/H+ in a collision is determined by the scattering angle χ

$$\Delta E \sim E \times (1 - cos\chi),$$

where E is the initial energy of the impacting proton or hydrogen atom. It is apparent that the energy loss for collisions in forward direction (for $\chi < 90°$) at small scattering angles χ is less than that for larger scattering angles. A key aspect of this kinetic MC model is the probabilistic treatment of the scattering angle distribution, which influences both the energy degradation rate and the angular redistribution of the precipitating protons and hydrogen atoms (Bisikalo et al., 2018; Shematovich et al., 2019). The kinetic model utilizes both total and differential cross sections when calculating the post-collision velocities for high-energy precipitating H/H+ and atmospheric particles. In the model, the most recent measurements or calculations of the required cross sections were adopted. The cross sections and scattering angle distributions for H/H+ collisions with CO2 are taken from Nakai et al. (1987) for charge exchange and stripping collisions, from Haider et al. (2002) for ionization, Lyman alpha and Balmer alpha excitation, and from Lindsay et al. (2005) for scattering angle distributions. The elastic and other inelastic collisions cross sections for H/H+ collisions with CO2 are assumed to be the same as for O2 (see, for details, Gérard et al. (2000)). The region under study is limited by the lower boundary, which is placed at 80 km, where H/H^+ particles are efficiently thermalized. The upper boundary is set at 500 km, where measurements or calculations of the precipitating fluxes of protons or hydrogen atoms are used as a boundary condition. Both table and/or analytic (Maxwellian and/or kappa-distribution) functions representing the energy spectra as well as the pitch-angle (monodirectional, isotropic, or limited by cone) distributions of precipitating particles could be used at the upper boundary. Detailed description of all modeled numerical aspects used for this kinetic MC model study could be found in recent papers (Bisikalo *et al.*, 2018; Shematovich *et al.*, 2019).

References:

Gérard J.-C., Hubert B., Bisikalo D.V., and Shematovich V.I. Lyman-alpha emission in the proton aurora. J. Geophys. Res., 2000, V. 105, No. A7, pp. 15795.

Shematovich V. I., D. V. Bisikalo, C. Diéval, S. Barabash, G. Stenberg, H. Nilsson, Y. Futaana, M. Holmstrom, and J.-C. Gérard. Proton and hydrogen atom transport in the Martian upper atmosphere with an induced magnetic field. J. Geophys. Res., 2011, V. 116, Issue A11, CiteID A11320.

Bisikalo D.V., Shematovich V.I., Gérard J.-C., Hubert B. Monte Carlo simulations of the interaction of fast proton and hydrogen atoms with the Martian atmosphere and comparison with in situ measurements. Journal of Geophysical Research: Space Physics, 2018, V. 123, Issue 7, pp. 5850-5861.

Shematovich V.I., Bisikalo D.V., Gérard J.-C., Hubert B. Kinetic Monte Carlo model of the precipitation of high-energy proton and hydrogen atoms into the Martian atmosphere with taking into account the measured magnetic field. Astronomy Reports, 2019, Vol. 63, No. 10, pp. 835–845.

Haider, S.A., Seth S. P., Kallio E., and Oyama K.I. Solar EUV and electron-proton-hydrogen atom-produced ionosphere on Mars: Comparative studies of particle fluxes and ion production rates due to different processes, Icarus, 2002, V. 159, pp. 18-30.

Lindsay, B. G., Yu W. S., and Stebbings R. F. Cross sections for electron capture and loss by keV oxygen atoms in collisions with CO and CO2, J. Geophys. Res., 2005, V. 110, pp. A02302.

Nakai, Y., Shirai T., Tabata T., and Ito R. Cross sections for charge transfer of hydrogen atoms and ions colliding with gaseous atoms and molecules, Atomic Data and Nuclear Data Tables, 1987, V.37, pp. 69-101.

Text S4.

Gronoff *et al.* 1-D Kinetic Model Description (Name: "Aeroplanets")

A. Introduction

The *Aeroplanets* model (Gronoff *et al.,* 2012a; Gronoff *et al.,* 2012b; Simon Wedlund *et al.* 2011) is a 1-D kinetic transport model computing the ionization and excitation of atmospheric species by photon, electron, proton, and cosmic ray impacts, including the effect of secondary particles (photoelectrons, secondary electrons and protoelectrons). It is based on the Trans* model series, initially developed for the Earth (Lilensten *et al.,* 1999; Lummerzheim and Lilensten 1994; Simon *et al.,* 2007 as Trans4), and subsequently adapted to Venus (Gronoff *et al.,* 2007, 2008), Mars (Witasse *et al.,* 2002, 2003; Simon *et al.,* 2009; Nicholson *et al.,* 2009), Titan (Gronoff, Lilensten, and Modolo 2009; Gronoff *et al.,* 2009a, 2009b), etc., and including several other modules such as a fluid model. Aeroplanets constitutes an improvement in modularity and adaptability over Trans4, with every separate module having the option of being turned off to study one specific aspect of particle precipitation in the atmosphere of planets.

The proton transport module is based on the work of Galand *et al.* (1997, 1998), Simon (2006) and Simon *et al.* (2007) for Earth, who solved semi-analytically the coupled proton-hydrogen dissipative kinetic transport equation for protons and hydrogen atoms charge-changing with neutral gas M:

$H^+ + M \rightarrow H + M^+ Electron\ capture, \sigma_{10}$ $H + M \rightarrow H^+ + M + e^- Electron\ loss/stripping, \sigma_{01}$.

It naturally includes angular redistributions due to magnetic mirror effects and to collisions (Galand *et al*., 1998)

B. Inputs and outputs

Inputs to the Aeroplanets model include cross sections, the vertical profile of atmosphere composition (*i.e*., composition at different altitudes), and the precipitating fluxes of particles such H and H^+ at the top of the atmosphere. Outputs include the vertical profile of H and H^+ differential energy fluxes, and the vertical profile of the production rate of excited and ionized species and electrons, including emissions. The produced photoelectrons can be plugged into the main Aeroplanets electron model as an external and additional source of ionization in the atmosphere.

Cross sections in Aeroplanets are taken from the latest version of the ATMOCIAD cross section and reaction rate database compiled and developed by Simon Wedlund *et al.* (2011), Gronoff *et al.* (2012a) and Gronoff *et al.* (2020), and freely available in Gronoff et al. (2021) In ATMOCIAD, experimental and theoretical cross

sections as well as their uncertainties are collected. Many proton-hydrogen impact cross sections have been discussed in the seminal works of Avakyan *et al.* (1998) and, in a lesser degree, of Nakai *et al. (*1987); they contain a critical review of processes for photons, e^-, H, H^+ colliding with various gases of aeronomic interest and have been fully integrated into ATMOCIAD.

Specifically, the proton transport code uses the following energy-dependent cross sections, process by process:

- **Elastic**. Parameterisations of Kozelov and Ivanov (1992) originally valid for (H^+, H) collisions with N_2, and assumed to be the same for CO_2 because of the lack of any recent measurements. The parameters are available in their Tables 1 and 2.
- **Ionization**. For H^+, Rudd *et al.* (1983) for high energies, extended at $E < 5$ keV by (Avakyan *et al.,* 1998). For H atoms, cross sections are based on Basu *et al.* (1987) for N_2 and on Avakyan *et al.* (1998) for the rescaling factor.
- **Electron capture ($H^+ \rightarrow H$)**. Kusakabe *et al.* (2000) for 0.2-4 keV protons, review by Avakyan *et al.* (1998) based on all other available data for higher energies (Desesquelles, Do Cao, and Dufay 1966; Barnett and Gilbody 1968; Toburen, Nakai, and Langley 1968; McNeal 1970; Rudd *et al.,* 1983 for $5 - 150$ keV). Note that recent sub-keV measurements have been made by Werbowy and Pranszke (2016) for CO and CO_2, although these are not yet implemented in the ATMOCIAD.
- **Electron loss ($H \rightarrow H^+$)**. Smith *et al.,* (1976) between $0.25 - 5$ keV, review by Avakyan *et al.,* (1998) using N_2 σ_{01} cross sections (Green and Peterson 1968) based on all other available data for higher energies.
- **Ly-α H($2p$) and H($2s$) states**. For both H^+ and H collisions, exciting state H($2p$) (Birely and McNeal 1972) corrected by factor 0.9 presumably because of observation angle issues as per the recommendation of Avakyan *et al.* (1998). For both impactors creating state H($2s$), factor 1.35 on the measurements of (Birely and McNeal 1972) is applied.

Although ATMOCIAD is an extensive collection of cross sections, there is still a rather poor characterization of cross sections at low energies (typically in the sub-keV range).

Regarding differential cross sections, Aeroplanets uses phase functions that are convolved with the energy-dependent cross sections above. For the particular cases computed for Step 1 of the present study, the following is used: for the two charge-transfer (10 and 01) and elastic cross sections, the screened Rutherford function is used, equal to that of the electrons with a screening parameter ϵ of 10^{-3} (this is the same as in Galand *et al.,* 1997, 1998 and Simon 2006, Simon *et al.,* 2007 for Earth's atmosphere):

$$\xi(cos\vartheta) = \frac{4\epsilon(1+\epsilon)}{(1+2\epsilon-cos\vartheta)^2}$$

with $\vartheta = \mu\mu' + \sqrt{1-\mu'^2}\sqrt{1-\mu^2}cos(\phi-\phi')$. μ and μ' are the cosine of the pitch angles before and after the collision, whereas ϕ and ϕ' are the azimuthal angles before and after the collision. For ionization, forward scattering is assumed following Galand *et al.,* (1998) for the Earth case.

Because of the seamless implementation of ATMOCIAD as input to Aeroplanets, other available sets of cross sections may be used. It is possible to estimate the

uncertainties from the cross sections using a Monte-Carlo approach as described in (Gronoff *et al.*, 2012a; Gronoff *et al.*, 2012b). The outputs of the proton-transport model are the ionization and dissociation rates (including excited states productions), the proton/H induced electron flux (which can be used in the electron model), and the proton/H fluxes at the different altitudes.

C. Implementation

The solution of the dissipative coupled Boltzmann H/H^+equation is based on the seminal work of Galand *et al.*, (1997, 1998), later developed and adapted as a module into Aeroplanets following Simon *et al.*, (2007). It is based on the idea that dissipative forces responsible for angular redistributions (due to elastic scattering) can be introduced in the force term of the generalized Boltzmann equation (Galand *et al.*, 1997). Rearranging the energy/angle terms of the H^+/H coupled system of equations leads to a linear system of equations parametrized by a large sparse square matrix A containing the energy degradation without angular redistributions of the incoming particle, for each altitude z so that:

$$\frac{\partial \Phi}{\partial z} = A\Phi + B$$

$\Phi = (\phi_{H^+}\ \phi_H)$ is the vector-flux of protons and hydrogen precipitating particles and B, the angular degradation term, is thus the term coupling downward and upward fluxes. Moreover, the mirror mode term can be switched on or off depending on the planet's configuration. The equation can be solved by calculating the exponential of matrix A for a typical grid of 100 energies and 10 angles, both of which can be increased by the user for better resolution.

In order to achieve such a feat of simplification for a complex system of equations, the following assumptions are made in the case of the Mars code: (i) plane parallel geometry, with the atmosphere stratified horizontally, and the pitch angle of the particles can be imposed, (ii) external forces neglected, (iii) steady-state fluxes, (iv) continuous slowing down approximation assumed because of the low energetic losses by the precipitating particles compared to the incident energy of the particles.

D. Strengths and applications

Aeroplanets is better qualified for the fast computation of the proton precipitation from a measured spectra near the planet, and for the fast computation of the whole effect of that precipitation thanks to its coupling with a secondary electron transport model. The analytic computation approach and assumed geometry prevent the computation within very complex magnetic topologies (which are best handled by Monte-Carlo models) but is well suited for handling large sets of initial angles and energies.

References:

Avakyan, S.V., R.N. Ii'In, V.M. Lavrov, and G.N. Ogurtsov. 1998. Collision processes and excitation of UV emission from planetary atmospheric gases: a handbook of cross sections. Taylor & Francis, Amsterdam.

Barnett, C. F., and H. B. Gilbody. 1968. "Measurements of Atomic Cross Sections in Static Gases." In Atomic Interactions Part a, edited by Benjamin Bederson and Wade L. Fite, 7:390.

Basu, B., J. R. Jasperse, R. M. Robinson, R. R. Vondrak, and D. S. Evans. 1987. “Linear transport theory of auroral proton precipitation: A comparison with observations.” J. Geophys. Res. 92 (A6): 5920–32. https://doi.org/10.1029/JA092iA06p05920.

Birely, J. H., and R. J. McNeal. 1972. “Lyman-Alpha Emission Cross Sections for Collisions of 1-25 keV H^+ and H with CO, CO_2, CH_4, and NH_3.” J. Chem. Phys. 56 (5): 2189–94. https://doi.org/10.1063/1.1677518.

Desesquelles, J., G. Do Cao, and M. Dufay. 1966. “Etude de l’ionisation de quelques gaz par des ions accélérés H^+ et H_2^+.” C. R. Acad. Sci. Paris 262 (B): 1329–32.

Galand, M., J. Lilensten, W. Kofman, and D. Lummerzheim. 1998. “Proton transport model in the ionosphere. 2. Influence of magnetic mirroring and collisions on the angular redistribution in a proton beam.” Annales Geophysicae 16 (October): 1308–21. https://doi.org/10.1007/s00585-998-1308-y.

Galand, M., J. Lilensten, W. Kofman, and R. B. Sidje. 1997. “Proton transport model in the ionosphere 1. Multistream approach of the transport equations.” Journal of Geophysics Research 102 (September): 22261–72. https://doi.org/10.1029/97JA01903.

Green, A. E. S., and L. R. Peterson. 1968. “Energy loss functions for electrons and protons in planetary gases.” J. Geophys. Res. 73 (1): 233. https://doi.org/10.1029/JA073i001p00233.

Gronoff, G., J. Lilensten, C. Simon, O. Witasse, R. Thissen, O. Dutuit, and C. Alcaraz. 2007. “Modelling Dications in the Diurnal Ionosphere of Venus.” Astronomy and Astrophysics 465 (April): 641–45. http://adsabs.harvard.edu/abs/2007A%26A...465..641G.

Gronoff, G., J. Lilensten, C. Simon, M. Barthélemy, F. Leblanc, and O. Dutuit. 2008. “Modelling the Venusian Airglow.” Astronomy and Astrophysics 482 (May): 1015–29. http://adsabs.harvard.edu/abs/2008A%26A...482.1015G.

Gronoff, G., J. Lilensten, L. Desorgher, and E. Flückiger. 2009a. “Ionization Processes in the Atmosphere of Titan. I. Ionization in the Whole Atmosphere.” Astronomy and Astrophysics 506 (November): 955–64. http://adsabs.harvard.edu/abs/2009A%26A...506..955G.

Gronoff, G., J. Lilensten, and R. Modolo. 2009b. “Ionization Processes in the Atmosphere of Titan. II. Electron Precipitation Along Magnetic Field Lines.” Astronomy and Astrophysics 506 (November): 965–70. http://adsabs.harvard.edu/abs/2009A%26A...506..965G.

Gronoff, G., C. Simon Wedlund, C. J. Mertens, and R. J. Lillis. 2012a. “Computing uncertainties in ionosphere-airglow models: I. Electron flux and species production uncertainties for Mars.” *Journal of Geophysical Research: Space Physics*, 117 (April): 4306, 18 PP., https://doi.org/10.1029/2011JA016930.

Gronoff, Guillaume, Cyril Simon Wedlund, Christopher J. Mertens, Mathieu Barthélemy, Robert J. Lillis, and Olivier Witasse. 2012b. “Computing Uncertainties in Ionosphere-Airglow Models: II. The Martian Airglow.” J. Geophys. Res. 117 (May): 17 PP. https://doi.org/201210.1029/2011JA017308.

Gronoff, G., Arras, P., Baraka, S., Bell, J. M., Cessateur, G., Cohen, O., Curry, S. M., Drake, J. J., Elrod, M., Erwin, J., Garcia-Sage, K., Garraffo, C., Glocer, A., Heavens, N. G., Lovato, K., Maggiolo, R., Parkinson, C. D., Simon Wedlund, C., Weimer, D. R., & Moore, W. B. (2020), Atmospheric Escape Processes and Planetary Atmospheric Evolution, Journal of Geophysical Research (Space Physics), 125(8), e27639, doi:10.1029/2019JA027639.

Kozelov, B. V., and V. E. Ivanov. 1992. "Monte Carlo calculation of proton-hydrogen atom transport in N $_2$." Plan. Space Sci. 40 (11): 1503–11. https://doi.org/10.1016/0032-0633(92)90047-R.

Kusakabe, Toshio, Kensuke Asahina, Jiang P. Gu, Gerhard Hirsch, Robert J. Buenker, Mineo Kimura, Hiroyuki Tawara, and Yohta Nakai. 2000. "Charge-transfer processes in collisions of H^+ ions with H_2, D_2, CO, and CO_2 molecules in the energy range 0.2-4.0 keV." Phys. Rev. A 62 (6): 062714. https://doi.org/10.1103/PhysRevA.62.062714.

Lilensten, J., P. L. Blelly, W. Kofman, and D. Alcaydé. 1999. "Auroral Ionospheric Conductivities: A Comparison Between Experiment and Modeling, and Theoretical F10.7-Dependent Model for EISCAT and ESR." Ann. Geophys. 14 (12): 1297–1304. https://doi.org/10.1007/s00585-996-1297-7.

Lummerzheim, D., and J. Lilensten. 1994. "Electron Transport and Energy Degradation in the Ionosphere: Evaluation of the Numerical Solution, Comparison with Laboratory Experiments and Auroral Observations." Annales Geophysicae 12 (November): 1039–51. http://adsabs.harvard.edu/abs/1994AnGeo..12.1039L.

McNeal, R. J. 1970. "Production of Positive Ions and Electrons in Collisions of 1-25-keV Protons and Hydrogen Atoms with CO, CO_2, CH_4, and NH_3." J. Chem. Phys. 53 (11): 4308–13. https://doi.org/10.1063/1.1673938.

Nakai, Y., T. Shirai, T. Tabata, and R. Ito. 1987. "Cross Sections for Charge Transfer of Hydrogen Atoms and Ions Colliding with Gaseous Atoms and Molecules." Atomic Data and Nuclear Data Tables 37 (January): 69. https://doi.org/10.1016/0092-640X(87)90005-2.

Nicholson, William P., Guillaume Gronoff, Jean Lilensten, Alan D. Aylward, and Cyril Simon. 2009. "A Fast Computation of the Secondary Ion Production in the Ionosphere of Mars." Monthly Notices of the Royal Astronomical Society 400 (November): 369–82. http://adsabs.harvard.edu/abs/2009MNRAS.400..369N.

Rudd, M. E., T. V. Goffe, R. D. Dubois, L. H. Toburen, and C. A. Ratcliffe. 1983. "Cross sections for ionization of gases by 5-4000-keV protons and for electron capture by 5-150-keV protons." Phys. Rev. A 28 (6): 3244–57. https://doi.org/10.1103/PhysRevA.28.3244.

Simon, C., J. Lilensten, J. Moen, J. M. Holmes, Y. Ogawa, K. Oksavik, and W. F. Denig. 2007. "TRANS4: a new coupled electron/proton transport code - comparison to observations above Svalbard using ESR, DMSP and optical measurements." Annales Geophysicae 25 (March): 661–73. https://doi.org/10.5194/angeo-25-661-2007.

555 Simon, C., O. Witasse, F. Leblanc, G. Gronoff, and J.-L. Bertaux. 2009. “Dayglow on
556 Mars: Kinetic Modelling with SPICAM UV Limb Data.” Planetary and Space
557 Science 57 (July): 1008–21.
558 http://adsabs.harvard.edu/abs/2009P%26SS...57.1008S.

559 Simon, Cyril. 2006. “Contribution à L’étude Des Entrées d’énergie Solaire Dans
560 L’ionosphère : Ions Doublement Chargés et Transport Cinétique Des Protons -
561 Application à La Terre et à Titan.” PhD thesis, Université Joseph-Fourier -
562 Grenoble I. http://tel.archives-ouvertes.fr/tel-00109802.

563 Simon Wedlund, C., G. Gronoff, J. Lilensten, H. Ménager, and M. Barthélemy. 2011.
564 “Comprehensive calculation of the energy per ion pair or W values for five major
565 planetary upper atmospheres.” Annales Geophysicae 29 (January): 187–95.
566 https://doi.org/10.5194/angeo-29-187-2011.

567 Smith, K. A., M. D. Duncan, M. W. Geis, and R. D. Rundel. 1976. “Measurement of
568 electron loss cross sections for 0.25- to 5-keV hydrogen atoms in atmospheric
569 gases.” J. Geophys. Res. 81 (13): 2231.
570 https://doi.org/10.1029/JA081i013p02231.

571 Toburen, L. H., M. Y. Nakai, and R. A. Langley. 1968. “Measurement of High-Energy
572 Charge-Transfer Cross Sections for Incident Protons and Atomic Hydrogen in
573 Various Gases.” Physical Review 171 (1): 114–22.
574 https://doi.org/10.1103/PhysRev.171.114.

575 Werbowy, S., and B. Pranszke. 2016. “Charge-exchange processes in collisions of
576 H^+,H_2^+,H_3^+,He^+ , and He_2^+ ions with CO and CO_2 molecules at energies below
577 1000 eV.” Phys. Rev. A 93 (2): 022713.
578 https://doi.org/10.1103/PhysRevA.93.022713.

579 Witasse, O., O. Dutuit, J. Lilensten, R. Thissen, J. Zabka, C. Alcaraz, P.-L. Blelly, *et al.*,
580 2002. “Prediction of a CO22+ Layer in the Atmosphere of Mars.” Geophysical
581 Research Letters 29 (April): 104–1.
582 http://adsabs.harvard.edu/abs/2002GeoRL..29h.104W.

583 Witasse, O., O. Dutuit, J. Lilensten, R. Thissen, J. Zabka, C. Alcaraz, P.-L. Blelly, *et al.*,
584 2003. “Correction to ‘Prediction of a CO22+ Layer in the Atmosphere of Mars’.”
585 Geophysical Research Letters 30 (April): 12–11.
586 http://adsabs.harvard.edu/abs/2003GeoRL..30g..12W.
587

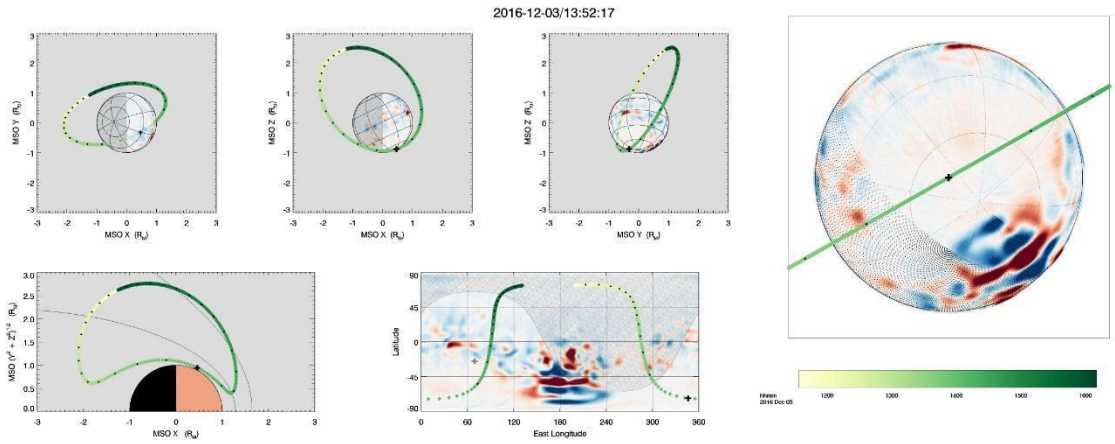

Figure S1. MAVEN spacecraft orbit information showing the locations of the spacecraft during Orbit 4235. The red/blue colors represent the magnitude and orientation of the crustal magnetic fields (see MAVEN PDS or Science Data Center website for more information). Note that the location of the periapsis is in the southern hemisphere and does not pass over any strong crustal magnetic fields.

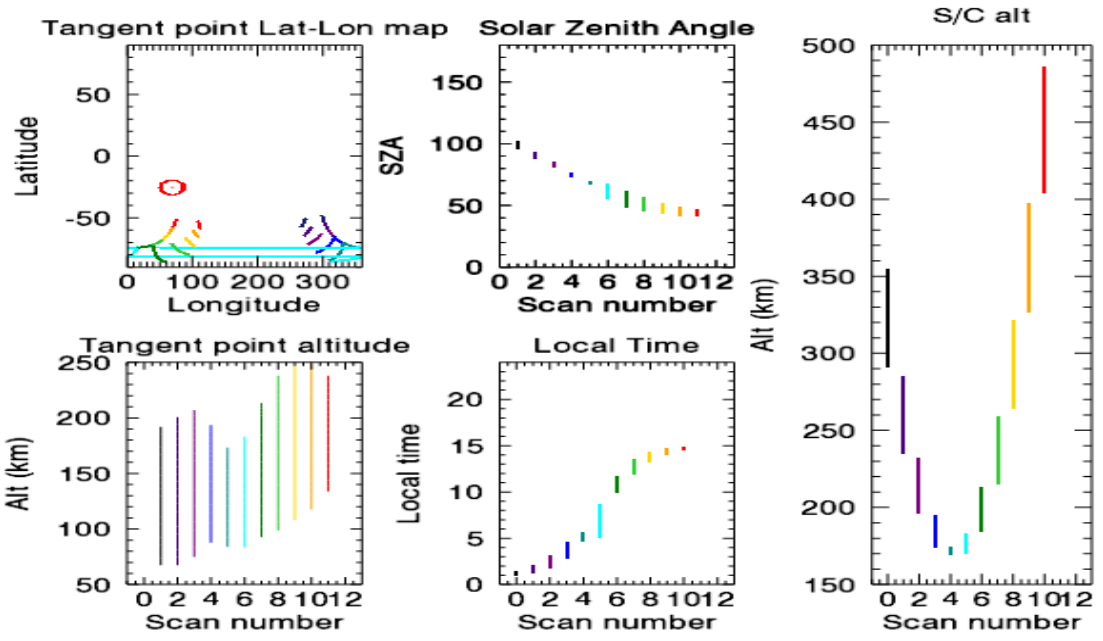

Figure S2. MAVEN/IUVS information showing ephemeris data for the IUVS limb scans during Orbit #4235 periapsis. Note that the location of periapsis is primarily on the dayside of the planet (with the exception of a few limb scan observations near the terminator) in the southern hemisphere and does not pass over any strong crustal magnetic fields. Different limb scans are marked by different colors within the orbit.

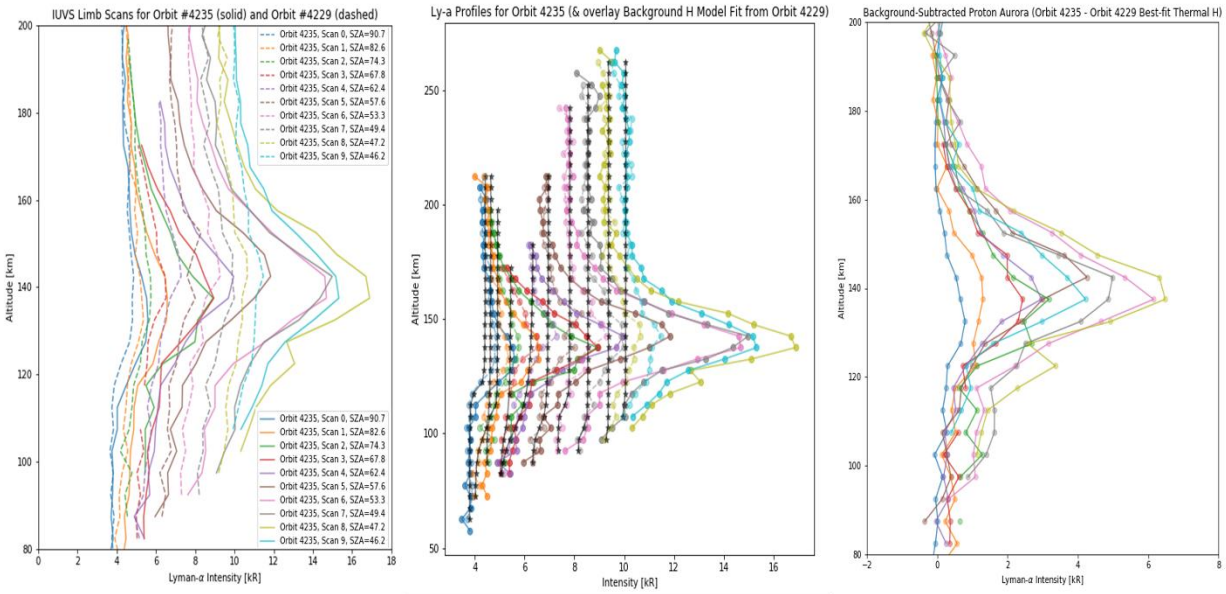

Figure S3. Altitude-intensity profiles and estimated heuristic thermal H background used for the background subtraction method described in this study. **Left**: IUVS Ly-α profiles for the orbit used in the data-model comparison (#4235), and a nearby orbit with little/less proton aurora activity (#4229) used to create the best-fit heuristic background coronal H profiles for each limb scan; peak profile SZAs for each scan in the two orbits are provided in the legend. **Middle**: Heuristic background thermal H profiles estimated from orbit #4229 (black profiles) overlain on Ly-α profiles for corresponding SZA limb scans in orbit #4235. **Right**: Final background-subtracted profiles that represent the contribution from only H-ENAs in the IUVS proton aurora observation in this orbit (*i.e.*, removing the background contribution from coronal thermal H).

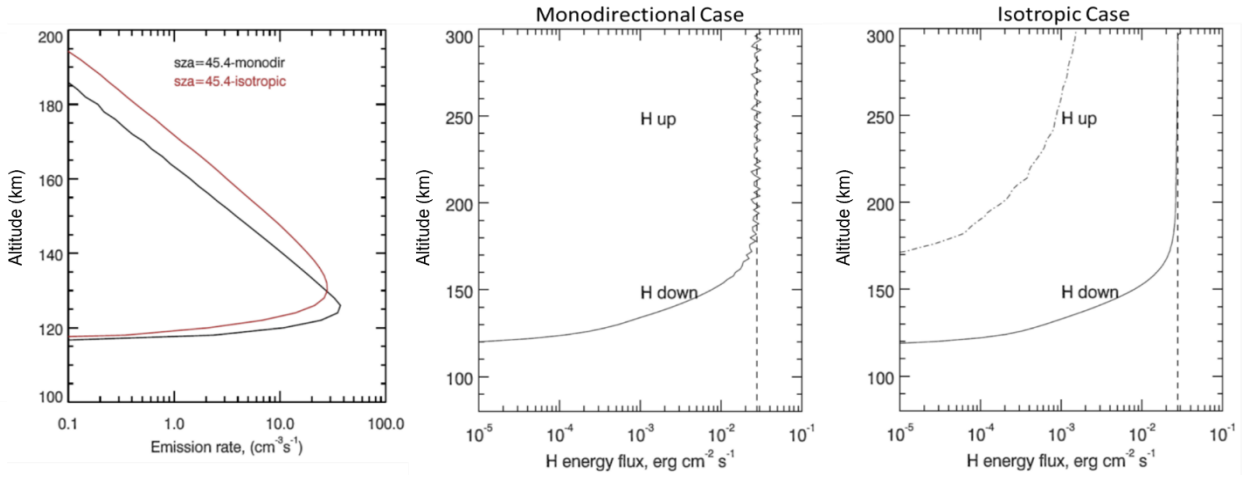

Figure S4. Example comparison of assuming monodirectional movement of the incident particle population in the atmosphere versus isotropic (simulation results from the Bisikalo/Shematovich *et al*. model). **Left:** Comparison proton aurora profiles using each assumption; **Middle:** Simulated H energy flux in the downward and upward (zero in this case) directions using a monodirectional assumption; **Right:** Simulated H energy flux in the downward and upward directions using an isotropic assumption. The simulated proton aurora profile using the isotropic assumption has a higher peak altitude and smaller VER due to the larger upward H population. The models in this study assume monodirectional particle movement, which could in turn lead to some of the observed discrepancies between the data and the models in Step 2 of the campaign. We note that neither of these two extreme assumptions (*i.e*., purely monodirectional or purely isotropic incident particle movement) is a probable physical occurrence, and the actual particle precipitation pattern is somewhere between these two limiting cases.

Cross Section (CS) Processes:	Elastic		Charge Exchange/ e^- Capture		e^- Stripping		Ionization		Lyman-α		Lyman-β &/or Lyman-γ		Balmer-α		Excitation of CO_2		Differential Scattering Cross Sections (DSCS)	
	$H\text{-}CO_2$	$H^+\text{-}CO_2$	$H\text{-}CO_2$	$H^+\text{-}CO_2$	$H\text{-}CO_2$	$H^+\text{-}CO_2$	$H\text{-}CO_2$	$H^+\text{-}CO_2$	$H\text{-}CO_2$	$H^+\text{-}CO_2$	$H\text{-}CO_2$	$H^+\text{-}CO_2$	$H\text{-}CO_2$	$H^+\text{-}CO_2$	$H\text{-}CO_2$	$H^+\text{-}CO_2$	$H\text{-}CO_2$	$H^+\text{-}CO_2$
Jolitz:	Newman+ 1986 [for $H/H^+ - N_2$]			Barnett+ 1977	Nakai+ 1987		Van Zyl+, 1978 [for $H - O_2$] McNeal, 1970 [rescaling]	Rudd+ 1985	Van Zyl & Neumann [for $H - O_2$] Birely & McNeal, 1971 [rescaling]	Avakyan+ 1998 [for $H^+ - O_2$] Birely & McNeal, 1971 [rescaling]			x	x			Newman+ 1986 Noel and Prölss, 1993 [for $H/H^+ - O_2$]	
Kallio:	Newman+ 1986 [for $H/H^+ - N_2$]			Rees, 1989 [for $H^+ - O_2$]	Van Zyl+, 1978 [for $H - O_2$]		Van Zyl+, 1978 [for $H - O_2$]	Rudd+ 1985	Van Zyl & Neumann, 1988 [for $H/H^+ - O_2$]				x	x			Newman+ 1986 Noel and Prölss, 1993 [for $H/H^+ - O_2$]	
Bisikalo/ Shematovich *et al.*:	Porter+ 1976			Nakai+ 1987 [for $H - O_2$ and rescaled]	Nakai+ 1987 [for $H - O_2$ and rescaled]		Haider+ 2002 [for $H - O_2$ and rescaled]		Haider+ 2002 [for $H - O_2$ and rescaled]				x	x			Lindsay+ 2005 [for $H/H^+ - O_2$ and rescaled]	
Gronoff *et al.*:	Kozelov & Ivanov, 1992 [for $H/H^+ - N_2$]			Kusakabe+ 2000 Avakyan+ 1998	Smith+ 1976 Avakyan+ 1998 [for $H - N_2$]		Basu+ 1987 [for $H - N_2$] Avakyan+ 1998 [rescaling]	Rudd+ 1983 Avakyan+ 1998	Birely & McNeal, 1972 [rescaled as per Avakyan+ 1998]		x	x			x	x	Avakyan+ 1998 Basu+ 1987 [Calculated from pitch angle using Rutherford-type collision functions]	

Table S1. List of cross sections (CS) that each model in this study may include. The five overlapping CS processes of each modeling team are shown in green, along with relevant references for those CS processes and Differential Scattering Cross Sections (DSCS). Bins marked with an "X" represent additional CS processes that can be included in models.